UC Berkeley
UC Berkeley Previously Published Works

Title

A 2.5 per cent measurement of the growth rate from small-scale redshift space clustering of SDSS-III CMASS galaxies

Permalink

https://escholarship.org/uc/item/9tp8p972

Journal

Monthly Notices of the Royal Astronomical Society, 444(1)

ISSN

0035-8711

Authors

Reid, Beth A
Seo, Hee-Jong
Leauthaud, Alexie
et al.

Publication Date

2014-10-11

DOI

10.1093/mnras/stu1391

Peer reviewed

A 2.5% measurement of the growth rate from small-scale redshift space clustering of SDSS-III CMASS galaxies

Beth A. Reid[1,2,3]⋆, Hee-Jong Seo[3,4], Alexie Leauthaud[5], Jeremy L. Tinker[6], Martin White[1,7]

[1] *Lawrence Berkeley National Laboratory, 1 Cyclotron Road, Berkeley, CA 94720, USA*
[2] *Hubble Fellow*
[3] *Berkeley Center for Cosmological Physics, LBL and Department of Physics, University of California, Berkeley, CA, 94720, USA*
[4] *Center for Cosmology and Astro-Particle Physics, Ohio State University, Columbus, OH 43210, USA*
[5] *Kavli Institute for the Physics and Mathematics of the Universe, Todai Institutes for Advanced Study, the University of Tokyo, Kashiwa, Japan 277-8583*
[6] *Center for Cosmology and Particle Physics, Department of Physics New York University, USA*
[7] *Departments of Physics and Astronomy, University of California, Berkeley, CA, 94720, USA*

18 July 2014

ABSTRACT
We perform the first fit to the anisotropic clustering of SDSS-III CMASS DR10 galaxies on scales of $\sim 0.8 - 32 \, h^{-1}$ Mpc. A standard halo occupation distribution model evaluated near the best fit Planck ΛCDM cosmology provides a good fit to the observed anisotropic clustering, and implies a normalization for the peculiar velocity field of $M \sim 2 \times 10^{13} \, h^{-1} \, M_{\odot}$ halos of $f\sigma_8(z = 0.57) = 0.450 \pm 0.011$. Since this constraint includes both quasi-linear and non-linear scales, it should severely constrain modified gravity models that enhance pairwise infall velocities on these scales. Though model dependent, our measurement represents a factor of 2.5 improvement in precision over the analysis of DR11 on large scales, $f\sigma_8(z = 0.57) = 0.447 \pm 0.028$, and is the tightest single constraint on the growth rate of cosmic structure to date. Our measurement is consistent with the Planck ΛCDM prediction of 0.480 ± 0.010 at the $\sim 1.9\sigma$ level. Assuming a halo mass function evaluated at the best fit Planck cosmology, we also find that 10% of CMASS galaxies are satellites in halos of mass $M \sim 6 \times 10^{13} \, h^{-1} \, M_{\odot}$. While none of our tests and model generalizations indicate systematic errors due to an insufficiently detailed model of the galaxy-halo connection, the precision of these first results warrant further investigation into the modeling uncertainties and degeneracies with cosmological parameters.

Key words: cosmology: large-scale structure of Universe, cosmological parameters, galaxies: haloes, statistics

1 INTRODUCTION

The clustering of galaxies on small scales provides important constraints on the relationship between galaxies and the underlying dark matter distribution. This relation is of interest in itself as a constraint on galaxy formation and evolution, as well as for quantifying the impact of galaxy-formation scale physics on larger scale clustering measures used for cosmological parameter constraints. Modern approaches to modeling the relationship between galaxies and the underlying dark matter distribution rely on the basic tenet that galaxy formation requires a gravitationally-bound dark matter halo or sub-halo to accumulate and condense gas (Peacock & Smith 2000; Seljak 2000; Benson et al. 2000; White, Hernquist, & Springel 2001; Berlind & Weinberg 2002; Cooray & Sheth 2002; Yang, Mo, & van den Bosch 2003). In their simplest form,

such "halo models" contain one dominant variable that determines the probability that a (sub-)halo hosts a galaxy of interest. In the halo occupation distribution (HOD) formalism adopted in this paper, halo mass is the dominant variable and halos are permitted to host more than one galaxy. In the sub-halo abundance matching ("SHAM") formalism, the maximum circular velocity at accretion is often used (Marinoni & Hudson 2002; Vale & Ostriker 2006; Conroy, Wechsler, & Kravtsov 2006). The primary advantage of SHAM is that each sub-halo hosts only a single galaxy, thus requiring fewer free parameters to specify the model but assuming a specific but physically motivated relation between central and satellite galaxies. The practical disadvantage is that *N*-body simulations require higher resolution to resolve sub-halos. In principle both of these approaches could be generalized to include additional secondary variables such as halo formation time, with observable consequences (Gao et al. 2005; Wang et al. 2013; Zentner, Hearin, van den Bosch 2013; Cohn & White 2013).

⋆ E-mail: beth.ann.reid@gmail.com

There are a host of observables available to constrain halo models as a function of galaxy properties: one-point statistics like number density or luminosity functions, two- or three-point galaxy clustering (Zehavi et al. 2011; Marin 2011), marked statistics (Sheth 2005; White & Padmanabhan 2009) and direct measurements the galaxy group multiplicity function (Yang, Mo, & van den Bosch 2009; Reid & Spergel 2009). The most widely used observable is the projected correlation function, w_p, which removes sensitivity to redshift space distortions by integrating over the line-of-sight separation. While redshift space distortion effects are more difficult to model, they do provide complementary constraints both on the velocity distribution of galaxies relative to their host dark matter halos (van den Bosch et al. 2005) and on cosmological parameters (Yang et al. 2004).

The primary goal of the present paper is to use the information in the anisotropy of the galaxy correlation function on scales $\sim 0.8 - 32\ h^{-1}$ Mpc to simultaneously constrain the HOD and growth rate of cosmic structure through the pairwise infall of galaxies caused by their mutual gravitational attraction (Kaiser 1987). Constraints on gravitational infall on these scales is of particular interest in searching for signatures of modified gravity: for instance, an $f(R)$ model with $|f_{R0}| = 10^{-4}$ predicts a $\sim 25\%$ increase in the amplitude of pairwise infall velocities on scales of 10-30 Mpc (Keisler 2013; Zu et al. 2013; Lam et al. 2012). Alternatively, the non-linear regime is also a promising avenue for constraining dark sector coupling (Piloyan et al. 2014). We can also use the constraints on the HOD to infer the nuisance parameter $\sigma^2_{\rm FOG}$ employed in our analysis on larger scales (Reid et al. 2012; Samushia et al. 2013) to account for the velocity dispersions of galaxies relative to their host dark matter halos. See Hikage (2014) for a similar concept applied to the power spectrum multipoles.

In this paper we focus on the CMASS sample from the SDSS-III Baryon Oscillation Spectroscopic Survey (BOSS). This sample has thus far been the focus of several cosmological analyses, most recently providing a one per-cent absolute distance measurement using the baryon acoustic oscillation (BAO) standard ruler (Anderson et al. 2013) and a 6% constraint on the growth rate of cosmic structure (Samushia et al. 2013; Beutler et al. 2013; Sanchez et al. 2013; Chuang et al. 2013). The projected correlation function of these galaxies has also been used to constrain halo models using both the HOD (White et al. 2011; Guo et al. 2014) and SHAM (Nuza et al. 2013) formalisms; this work represents the first quantitative comparison to the small-scale anisotropic clustering of the CMASS galaxies.

The layout of the paper is as follows. In Sec. 2 we describe the basic conceptual elements of our analysis. Sec. 3 details our dataset, while Sec. 4 focuses on mitigating the impact of fiber collisions in our spectroscopic galaxy sample. Sec. 5 presents fiber-collision corrected measurements and uncertainties. Sec. 6 presents the details of our N-body simulation based HOD model that we use to fit the observed anistropic CMASS galaxy clustering. The principal results of a simultaneous fit to the HOD parameters and $f\sigma_8$ are presented in Sec. 7. In Sec. 8 we discuss the implications of our results for constraining modified gravity models, and in Sec. 9 we discuss future prospects for this technique.

2   PRELIMINARIES

2.1   Analysis Road Map

Many components of our analysis are interdependent, so a strictly linear presentation is impossible. Therefore we provide an overview of the full analysis here. The first new product of this work is an unbiased estimate of the small-scale aniostropic clustering of the CMASS sample from the BOSS survey. Second, we implement a new algorithm to quickly and accurately predict two-point clustering statistics as a function of HOD parameters. The algorithm is based directly on measuring the clustering of halo catalogs derived from N-body simulations; it uses no analytic approximations or fits for the one-halo or two-halo terms. We combine these two products to constrain both HOD and growth rate parameters.

For the measurements, the primary source of systematic uncertainty, referred to as "fiber collisions", is the instrumental constraint that spectroscopic fibers cannot be placed closer than 62" during a single observation. Therefore, the galaxies that do not receive a spectroscopic fiber are a non-random subset of the targets; they preferentially reside in regions of higher target density. Moreover, the positioning of spectroscopic tiles depends on the angular density of targets, so that regions in which plates overlap (and therefore fiber collisions can be resolved) are not representative of the full survey. Ignoring these effects would substantially bias our clustering measurements. In Sec. 4 we consider two fiber collision correction methods previously introduced in the literature: nearest neighbor redshift assignment and angular upweighting. Neither correction is exact, so we apply the BOSS tiling pipeline to a mock galaxy catalog to determine which fiber collision correction method is best on which scales, which potential observable is the least affected, and what the residual biases are. Below we define the set of clustering measures we will consider for our final analysis.

We make use of halo catalogs derived from different N-body simulations for three distinct purposes:

- to evaluate theoretical models for parameter estimation
- to estimate the uncertainty (theory covariance matrix) due to the finite volume of simulations used to compute the theoretical models
- to generate the mock galaxy catalog to which we applied the BOSS tiling algorithm in order to study the effects of fiber collisions.

Below we specify the set of N-body simulations we use for these purposes as well as explain how the halo catalogs are derived from the simulation outputs.

The primary goal of our analysis is to constrain the growth rate of cosmic structure using redshift space distortions, and so we review the basic physics first.

2.2   Redshift Space Distortions (RSD)

Because cosmological flows are non-relativistic, the spectrosopically observed redshift of a galaxy can be expressed as the sum of two components:

$$z_{\rm spec} = z_{\rm cosmo} + \frac{v_{\rm p}^{\rm LOS}}{ac} \tag{1}$$

where $z_{\rm cosmo}$ is the redshift expected if the universe were homogeneous, while the second term accounts for the component of the physical "peculiar velocity" along the line-of-sight (LOS), i.e., the proper motion of an object due to its local gravitational potential. Here $a = 1/(1 + z_{\rm cosmo})$ is the scale factor of the universe and c is the speed of light. "Redshift space distortions" (RSD) is the generic term referring to distortions in the observed galaxy density field due to the $v_{\rm p}^{\rm LOS}$ contribution to the observed redshift coordinate. Throughout this work we will quote velocities in units of distance,

with the relation between peculiar velocity v_p and apparent line-of-sight comoving distance shift Δs for a galaxy observed at a given by

$$\Delta s = \frac{v_p^{LOS}}{aH(a)}, \qquad (2)$$

where $H(a) = \dot{a}/a$ is the expansion rate at a.

On large scales where linear perturbation theory applies, the peculiar velocity field $\mathbf{v}_p$ is simply related to the underlying matter density fluctuations, δ_m:

$$\nabla \cdot \mathbf{v}_p = -aHf\delta_m \qquad (3)$$

where $f = \mathrm{d}\ln D/\mathrm{d}\ln a$ is the logarithmic growth rate, and $D(a)$ is the linear growth function that specifies the amplitude of fluctuations as a function of a, relative to some initial fluctuation amplitude: $\delta_m(a) \propto D(a)\delta_{m,i}$. Therefore, in the linear regime, a measure of the amplitude of the peculiar velocity field through RSD provides a constraint on f times the amplitude of matter fluctuations on some scale; often this scale is taken to be 8 h^{-1} Mpc, so that linear redshift space distortions measure $f\sigma_8$. Because the scale-dependence of the matter power spectrum is extremely well-constrained by the CMB, the specified scale is not important for many applications (see Section 5.1 of Reid et al. 2012). The measurement of the amplitude of the peculiar velocity field is typically made using the variation of the amplitude of galaxy clustering as a function of orientation with respect to the line of sight caused by redshift space distortions. On large scales, Eq. 3 implies (Kaiser 1987)

$$\delta_g^s(\mathbf{k}) = (b + f\mu^2)\delta_m^r(\mathbf{k}). \qquad (4)$$

Here δ_g^s is the observed (in "redshift space") galaxy density fluctuation for wavevector $\mathbf{k}$, b is the real space linear galaxy bias, and $\delta_m^r(\mathbf{k})$ is the true underlying matter density fluctuation (i.e., in "real space", without velocity perturbations included in the redshift direction coordinate). The parameter μ is the cosine of the angle between $\mathbf{k}$ and the LOS, and the known μ dependence allows a measurement of $f\sigma_8$ after marginalizing over the unknown galaxy bias. In the present work, we work strictly in configuration space; see Fisher (1995) for the configuration space equivalent of Eq. 4.

On smaller scales investigated in the present work, nonlinearities become important and the relationship between $\mathbf{v}$ and δ_m becomes substantially more complicated. A detailed description of many distinct physical effects that impact the observed redshift space galaxy clustering on small scales is given in Tinker (2007). Because of the complexity of the modeling and the high statistical precision of our data, we resort to N-body simulations to provide predictions for our observables, which we describe below.

2.3 Two-dimensional correlation function $\xi(r_\sigma, r_\pi)$

Because RSD effects only distort the observed coordinates (or pair separations) in the LOS direction, the two-point correlation function ξ is fundamentally a function of two variables. In Fig. 1 we choose as coordinates the LOS separation, r_π, and the separation transverse to the LOS, r_σ to display our measurement from the galaxy sample analysed in the present work. This measurement uses the angular upweighting method described in Sec. 4.1 to correct for fiber collisions. Two primary features are apparent: on large scales ($\sim 8\ h^{-1}$ Mpc and above), contours of constant ξ are "squashed" in the LOS direction. The correlation between the density and velocity field described by Eq. 3 on average reduces the apparent separation between pairs of galaxies along the line of sight.

On smaller scales where Eq. 3 breaks down, the contours are instead stretched along the LOS. Galaxies orbiting in the potential of a gravitationally bound dark matter halo have a virial-like velocity component. As we will see, the SDSS-III CMASS galaxies shown here occupy massive dark matter halos with large virial velocities. The prominent feature in ξ along the LOS (i.e., at $r_\sigma < 1\ h^{-1}$ Mpc) is due to these motions, often called "fingers-of-god" (FOGs) (Jackson 1972); note that these virial-like velocities distort ξ at all separations, and their impact must be mitigated even in analysis of relatively large scales (e.g., Reid et al. 2012).

In this work we choose not to analyse $\xi(r_\sigma, r_\pi)$ directly, since information is spread over a large number of bins. As described in Sec. 5.1, we estimate measurement errors by bootstrapping the survey, and therefore need to reduce the number of measurements to well below the number of bootstrap regions, which are limited in number since each region must span scales larger than we include in our analysis. In this section we present the observables we will estimate from $\xi(r_\sigma, r_\pi)$ and compare with theoretical models directly.

The most widely used observable in studies of small-scale galaxy clustering is $w_p(r_\sigma)$, which quantifies the clustering as a function of transverse pair separation r_σ. All pairs with line-of-sight separations smaller than π_{max} contribute to w_p:

$$w_p(r_\sigma) = 2 \int_0^{\pi_{max}} dr_\pi \xi(r_\sigma, r_\pi). \qquad (5)$$

π_{max} is traditionally chosen to be large (80 h^{-1} Mpc in this work) so that the sensitivity of w_p to redshift space distortions is minimal (but see van den Bosch et al. 2013).

On large scales and for the highly biased tracers we consider here, the majority of redshift space information is available by measuring the first two even multipoles ($\ell = 0, 2$) of ξ:

$$\xi_\ell(s_i) = \frac{2\ell + 1}{2} \int d\mu_s\, \xi(s_i, \mu_s)L_\ell(\mu_s), \qquad (6)$$

where redshift space separation s is defined by $s^2 = r_\sigma^2 + r_\pi^2$ and $\mu_s = r_\pi/s$ is the cosine of the angle of the galaxy pair with respect to the line of sight. Here L_ℓ is the Legendre polynomial of order ℓ. Both our measurement and theoretical estimates of $\xi_{0,2}$ are computed by replacing the integral with a direct sum over bins of width $d\mu_s = 0.1$. Each bin in redshift space separation s_i is averaged over a finite band of separations.

To mitigate the effect of fiber collisions, our primary analysis uses the statistic $\hat{\xi}_{0,2}$ which approaches $\xi_{0,2}$ on large scales, but eliminates all bins that include pairs with $r_\sigma < 0.534\ h^{-1}$ Mpc. This choice corresponds to pairs separated by the fiber collision radius 62" at the maximum redshift included in our analysis, $z = 0.7$. Heuristically, we estimate

$$\hat{\xi}_\ell(s_i) = \frac{2\ell + 1}{2} \int_0^{\mu_{max}(s_i)} d\mu_s \xi(s, \mu_s)L_\ell(\mu_s). \qquad (7)$$

In practice, our implementation is slightly more complicated, but we emphasize that the measurement and theoretical predictions are computed with exactly the same algorithm, and so the details are irrelevant for the comparison of the two. We start with relatively fine logarithmic binning in s (d $log_{10}\ s = 0.035$) and μ (d$\mu_s = 0.005$) to compute $\xi(s, \mu)$. We then aggregate pair counts in the small s bins into larger bins for which we report our measurements. In the case where some of the small bins have r_σ larger than the cutoff, we estimate ξ in the larger s bin from only that subset of small bins. If none of the bins have large enough r_σ in the μ-bin, we set ξ for that bin to 0 before integrating over μ to estimate $\hat{\xi}_{0,2}$; this is equivalent
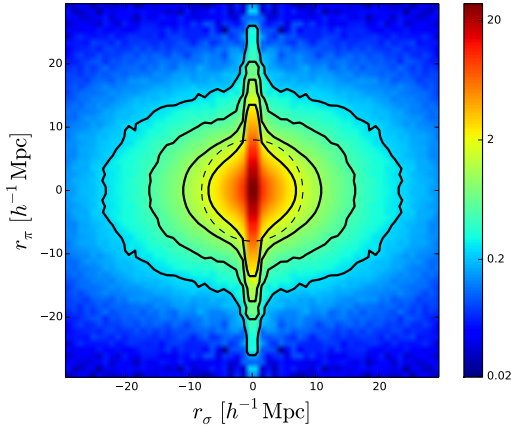
Figure 1. The two-dimensional correlation function $\xi(r_\sigma, r_\pi)$ of SDSS-III CMASS galaxies. The perturbations of the observed redshifts about the Hubble flow due to peculiar velocities introduce anistropy in the correlation strength with respect to the line of sight (y-axis in the figure). In this plot fiber collisions have been corrected using the angular upweighting method. The dashed circle indicates the separation scale ($\sim 8~h^{-1}$ Mpc) at which the observed quadrupole transitions from positive (dominated by Finger-of-God velocities) to negative (dominated by large scale Kaiser infall velocities). Contours at $\xi = [2, 1, 0.5, 0.25]$ are shown with solid black curves.

Table 1. Cosmological and simulation parameters for the N-body simulations used in this paper.

Parameter	LowRes	MedRes	HiRes
$L_{\rm box}$ (h^{-1} Mpc)	2750	1380	677.7
N_p	3000^3	2048^3	2048^3
m_p ($h^{-1}~M_\odot$)	5.86×10^{10}	2.5×10^{10}	3.10×10^9
Ω_m	0.274	0.292	0.30851
$\Omega_b h^2$	0.0224	0.022	0.022161
h	0.7	0.69	0.6777
n_s	0.95	0.965	0.9611
σ_8	0.8	0.82	0.8288
$z_{\rm box}$	0.550	0.550	0.547
$f\sigma_8(z_{\rm box})$	0.455	0.472	0.482

to only integrating up to a $\mu_{\rm max}$ that is different for each fine s bin. The previous step ensures that no pairs with r_σ smaller than the fiber collision scale are included. The exact s and μ boundaries for our final bins are listed in Table 3.

2.4 N-body simulation Halo Catalogs

We make use of three periodic N-body simulation sets throughout this paper. We have a single realization for the LowRes and HiRes cases, and three independent realizations (labelled 0,1,2) in the MedRes case. The simulation parameters are listed in Table 1. The LowRes box has parameters favored by WMAP7 (Komatsu et al. 2011), while the HiRes box adopts the "Planck+WP+highL+BAO" constraints from the Planck analysis (Planck Collaboration 2013); all N-body simulations assume massless neutrinos, while the parameter constraints from Planck assume $\sum m_\nu = 0.06$ eV. The Planck best fit and HiRes cosmologies will therefore have slightly different expansion and structure growth histories which should be negligible for the present application. The MedRes cosmology is "between" LowRes and HiRes. For each simulation we generate spherical overdensity (SO) halo catalogs using an overdensity of

$\Delta_m = 200$ relative to the mean matter density ρ_m to define the halo virial radius $r_{\rm vir}$. Our catalogs extend down to fifty particles per halo where necessary. We use the Tinker et al. (2008) implementation of the SO halo finder, which allows halo virial radii to overlap, as long as the center of one halo is not within the virial radius of another halo; this choice alters the halo-halo clustering on scales near $r_{\rm vir}$ compared with a friends-of-friends halo catalog, in which two such halos would be bridged into a single halo (see figure 9 of Reid & Spergel 2009).

More specifically, halos are identified around pseudo-peaks in the density field, which may or may not be located on the true density peak of the host halo. A radius $R_{\rm halo}$ is computed for each pseudo-peak in the density field within which the density is $200\rho_m$. Starting at a radius of 1/3 the initial $R_{\rm halo}$, the center of mass is computed within this restricted radius and iterated to convergence. If the pseudo-peak lies on a subhalo, this procedure migrates the halo center to the true host halo density peak. Once convergence is reached, the top-hat radius is incrementally reduced and the center of mass is recomputed until the top-hat radius is $R_{\rm halo}/15.9$ or the number of particles within the top-hat radius drops below 20. The center of mass is again computed iteratively at the tophat radius of $R_{\rm halo}/15.9$. For halos above the 20 particle limit, this algorithm averages over $\sim 3.7\%$ of all halo members. This algorithm was originally refined to accurately locate the halo center; we verified that it recovers the position of the potential minimum within the halo to within 0.01-0.02 h^{-1} Mpc. We denote the mean velocity of these densest particles as $\mathbf{v}_{\rm DENS}$, and is our fiducial choice for the velocity of each halo's central galaxy. This choice is by no means unique, and Appendix B shows that while there is strong evidence that the dense central region of the halo does have a bulk velocity with respect to the halo members, the rms offset between the "central" velocity and the center-of-mass velocity depends on the radius over which the average is taken. The effective radius for our $\mathbf{v}_{\rm DENS}$ definition ranges from 0.04 - 0.08 h^{-1} Mpc for halos with $M < 1.2 \times 10^{14}~h^{-1}~M_\odot$ in our MedRes simulation; this mass range hosts 90% of the central galaxies in our sample for our best fit halo occupation distribution model. The median seeing-corrected effective radius of CMASS targets is 1.2" (Masters et al. 2011), or 0.0087 h^{-1} Mpc. For a de Vaucouleurs profile, 0.04 (0.08) h^{-1} Mpc would contain 87% (96%) of the light. Therefore, our choice of central velocity definition is reasonably well matched to the typical extent of our target galaxies. Of course, since our simulations contain only dark matter, any impact of baryonic physics on the central dynamics has been neglected.

The LowRes box provides a volume much larger than the survey we analyse. To match the observed clustering strength using the LowRes box, we require halos below the SO halo catalog threshold; for this purpose, we use a friends-of-friends (FOF) algorithm with linking length 0.168 to identify halos (Davis et al. 1985), and then compute their masses in a spherical aperture at Δ_{180}. We further rescaled the FOF-derived halo masses by a factor of 0.975 to approximate Δ_{200} masses used in the SO catalogs. The FOF catalog extends down to $5.4 \times 10^{11}~h^{-1}~M_\odot$. Typically only $\sim 5\%$ of the mock galaxies are assigned to FOF-derived halos, so the impact of these details should be minimal. This hybrid catalog did show evidence for numerical artefacts in the halo clustering, which led us to adopt higher resolution simulations for our primary parameter constraints. The HiRes box provides more than sufficient mass resolution but its small volume made the theoretical predictions somewhat noisy. Because this box is smaller than our survey size, we have to add a theoretical error budget to the observational one. We use mock catalogs derived from the LowRes box for two

applications. First, we generate a mock catalog to which we apply the BOSS tiling algorithm in order to investigate the fiber collision effects on clustering (see Sec. 4). Second, we subdivide the LowRes box into 64 subboxes to estimate the theoretical uncertainty due to the finite volume of the HiRes box.

3 DATA

In this paper we analyse data included in data release 10 (DR10) of the Sloan Digital Sky Survey (SDSS; Gunn et al. 1998; York et al. 2000; Gunn et al. 2006; Eisenstein et al. 2011). We refer the reader to Ahn et al. (2013) for the full details about the DR10 dataset. Briefly, BOSS uses imaging data available in SDSS data release 8 (Aihara et al. 2011) to target quasars and two classes of galaxies for spectroscopy. The larger CMASS sample analysed in this work covers $0.4 < z < 0.8$, but as in Anderson et al. (2013) we restrict our analysis to the subsample falling within $0.43 < z < 0.7$. The LOWZ galaxy targets primarily have $z < 0.4$ and so we treat them as uncorrelated with the CMASS targets.

Errors in the redshift fitting to the BOSS spectra propagate as random errors in the LOS redshift space position of each galaxy. The median redshift error reported by the BOSS spectroscopic pipeline is 0.00014. Bolton et al. (2012) estimate that these errors are underestimated by $\sim 20\%$. While the redshift error increases with z (by 40% between the lower and upper third of the sample), the conversion to distance errors partially cancels this. We therefore expect a typical line-of-sight offset of 0.44 h^{-1} Mpc due to redshift errors. We incorporate redshift errors into our theoretical model by adding a random LOS offset to each mock galaxy that is drawn from a Gaussian distribution of width $\sigma = 0.44$ h^{-1} Mpc.

Throughout we treat the North and South galactic cap regions of the survey separately. Photometric calibration across the hemispheres is subject to systematic error, and may result in slightly different populations of galaxies being targeted in the two hemispheres; see Ross et al. (2012) for a more detailed analysis of potential differences. We will address the consistency of the north and south for each statistic we compute, and combine them before performing fits. The majority of our sample is contained in the north: 409365 of 521958 galaxies in the final sample.

In Anderson et al. (2013) we upweighted nearest neighbor galaxies to account for two potentially non-random sources of missing redshifts: fiber collisions and failure to obtain redshifts for targets assigned a spectroscopic fiber. We adopt the same weighting procedure for redshift failures in present work. For fiber collisions, we assign a nearest neighbor redshift to each collided galaxy, drawn from another CMASS target within the fiber collision group provided by the tiling algorithm. In total, we corrected for 7043 (2829) redshift failures in the north (south) and 24648 (6297) fiber collided galaxies. The survey completeness is treated as uniform in each sector, which is defined as a unique intersection of spectrosopic tiles. The angular mask is defined in the same way as in Anderson et al. (2013), except that for the purposes of fiber collision correction uniformity, we only retain sectors where all planned spectroscopic tiles have been observed. We track two values of completeness in each sector. For $c_{\rm NN}$, collided galaxies are assigned a nearest-neighbor redshift and treated as observed when estimating completeness. To define the completeness used in the angular upweighting method (Sec. 4.1), fiber collided galaxies are instead treated as a random subsample of the spectroscopic sample that lack redshifts, so they reduce the completeness of their sector. The area-weighted completenesses are $c_{\rm NN} = 0.988(0.984)$ and

$c_{\rm ang} = 0.936(0.939)$ in the north (south). Finally, we note that we neglect both the FKP and systematics weights adopted in Anderson et al. (2013) so that galaxies receive equal weight in both the angular and three-dimensional clustering measurements. The systematics weights primarily affect clustering on very large scales, and can therefore be neglected on the small scales of interest here.

In order to place the observed angular and redshift coordinates of each galaxy on a comoving grid, we adopt the same fiducial cosmological model as in Anderson et al. (2013): $\Omega_m = 0.274$. We compute ξ from the Landy-Szalay estimator (Landy & Szalay 1993), which depends on the data-data (DD), data-random (DR), and random-random (RR) pair counts in each separation bin of interest:

$$\xi(\Delta \mathbf{r}_i) = \frac{DD(\Delta \mathbf{r}_i) - 2DR(\Delta \mathbf{r}_i) + RR(\Delta \mathbf{r}_i)}{RR(\Delta \mathbf{r}_i)}. \qquad (8)$$

Random galaxies are an unclustered sample of points within the survey mask with the same sector-by-sector completeness as the data and with a radial selection function matched to the data by drawing the random galaxy redshifts from the observed ones (i.e., the "shuffle" method advocated in Ross et al. 2012). In contrast to some other works that use C^{-1} weighting, we combine clustering statistics estimated separately in the two hemispheres using a simple weighted average with weights proportional to the total galaxy weight in each hemisphere.

4 FIBER COLLISION CORRECTIONS

The tiling algorithm (Blanton et al. 2003) determines the location of the 3° spectroscopic tiles and allocates the available fibers among the galaxy and quasar targets. A physical constraint of the instrument is that fibers may not be closer than 62" on a given spectroscopic tile. The algorithm divides target galaxies into friends-of-friends groups with a linking length of 62", and then assigns fibers to the groups in a way that maximizes the number of targets with fibers. The choice of which galaxies are assigned the fibers is otherwise random. The algorithm adapts to the density of targets on the sky, with a net result being that regions covered by more than one tile have a larger than average number density. For the DR10 sample studied in this work, 42% (52%) of the area in the north (south) is covered by multiple tiles, and the number density is larger by 4.6% (3.1%) in those regions. For the final survey footprint, the enhancement is 5.1% in both the north and south. Fiber collisions are partially resolved only in the multiple tile regions, and therefore may not be representative of the unresolved fiber collisions in lower target density regions. For this reason we do not adopt the method of Guo, Zehavi, & Zheng (2012), which uses the overlap regions to correct fiber collisions in the single tile regions.

Fiber-collided galaxies cannot simply be accounted for by reducing the completeness of their sector, since they are a non-random subset of targets (conditioned to have another target within 62"). This is evident in Fig. 2, where we compare the redshift distribution of all good CMASS redshifts with the redshift distribution of the nearest neighbor of fiber collided galaxies; the latter preferentially reside near the peak of $p(z)$, where $\bar{n}(z)$ is also the largest. In this section we will apply the tiling algorithm to a mock galaxy catalog in order to assess the robustness of our fiber collision correction methods to the existence of realistic tile position-target density correlations. Finally, we note that fiber collisions also occur between CMASS targets and targets from other classes. Since quasar targets are given higher priority, we account for them by
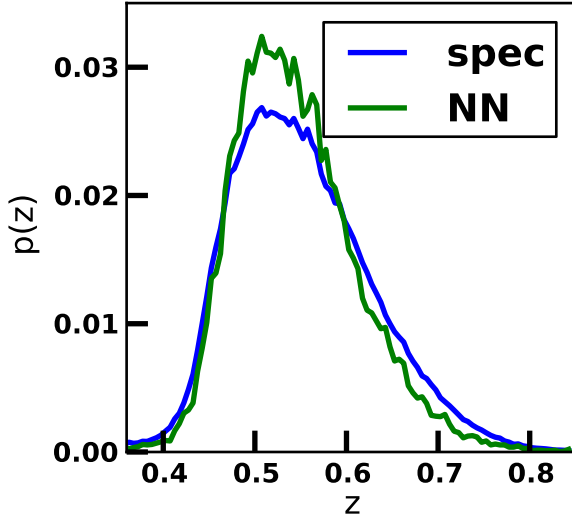
Figure 2. The normalized redshift probability distribution for CMASS targets that were assigned fibers (blue) and fiber collided galaxies (green). For collided galaxies, we use the nearest neighbor redshifts as a proxy; since the galaxy in a fiber collision pair that receives the fiber is randomly chosen, this is an unbiased estimate of the redshift distribution for objects without a fiber due to a fiber collision.

simply including a 62" veto mask around each high priority quasar target. CMASS targets that are fiber collided with LOWZ galaxies are treated as random losses; the completeness of their sectors is reduced accordingly, rather than assigning them a nearest neighbor redshift.

4.1 The angular upweighting method

The comparison of the angular clustering of the target galaxies with the angular clustering of the subsample of targets for which spectra were obtained quantifies the number of pairs lost as a function of angular separation due to fiber collisions. One common method to use this information to correct measurements of ξ is to first treat the fiber-collided missing galaxies as if they were a random subsample of targets (i.e., adjust the completeness of the sector based on the fraction of targets without spectra), and then to upweight DD pairs in the Landy-Szalay estimator (Eq. 8) using the following weight (Hawkins et al. 2003):

$$w_{\text{pair}}(\theta) = \frac{1 + w_s(\theta)}{1 + w_t(\theta)}. \qquad (9)$$

Here w_s is the angular correlation function of galaxies drawn from the "spectroscopic" sample for which you obtained redshifts and want to estimate ξ. w_t is the angular correlation function of the targets from which the spectroscopic sample is drawn.

As we will show using our tiled mock catalog, this method performs quite well at recovering the true clustering down to scales well below the BOSS fiber collision radius, and has been successfully applied in a number of other surveys (Hawkins et al. 2003; Li et al. 2006; Ross et al. 2007; White et al. 2011; de la Torre et al. 2013). However, there are a number of open issues and limitations of the method:

• The method assumes that the distribution of LOS separations of the fiber-collided pairs is the same as the distribution for non-collided pairs; this will not be true in detail, since fiber-collided pairs may occupy a different distribution of halo masses (and therefore have a different large-scale bias) compared to the full target sample. Since w_{pair} quickly approaches 1 on large scales, the method will not properly account for the possibility of fiber-collided galaxies having a larger bias. For this reason we prefer the next method (nearest neighbor redshift assignment) on scales well above the fiber collision scale.

• The weight given in Eq. 9 is not easily generalizable to "spectroscopic" samples that are subsets of the full set of fibers (in our case, cutting out stars and applying redshift boundaries), at least not without additional assumptions regarding the redshift dependence of the target galaxy clustering.

The Limber approximation (Limber 1954) allows us to relate the angular and real-space clustering given the probability distribution $p(\chi)$ that an object in the sample is at comoving distance χ.

$$w(\theta) = \int_0^\infty d\chi\, p^2(\chi) \int_{-\infty}^{+\infty} dr_z \xi(\sqrt{\chi^2\theta^2 + r_z^2}, \chi) \qquad (10)$$

Here r_z is the LOS separation between a pair. The explicit χ dependence of ξ in Eq. 10 indicates that ξ may evolve with redshift. We can only observe $w(\theta)$ for the full target sample. However, if we adopt a particular model for $\xi(r, \chi)$, then in principle we can fit for its parameters and infer the expected $w(\theta)$ for a subsample of targets occupying a narrower range of χ (i.e., different $p(\chi)$). The simplest choice is a power law correlation function, $\xi(r) = (r/r_0)^{-\gamma}$. In that case, Eq. 10 gives $w(\theta) = A_w \theta^{1-\gamma}$ with

$$A_w = \sqrt{\pi} r_0^\gamma \frac{\Gamma(\gamma/2 - 1/2)}{\Gamma(\gamma/2)} \int_0^\infty d\chi\, p^2(\chi) \chi^{1-\gamma}. \qquad (11)$$

For a more complicated $\xi(r)$, $w(\theta)$ in different redshift slices must generically have a different θ dependence that depends on $p(\chi)$. To relate the observed w_t to the one for the subsample entering Eq. 9, Hawkins et al. (2003) employed the Limber approximation, assuming a power law form for ξ and that it does not evolve with redshift. We make the same assumption in Sec. 5.2 but propagate the uncertainty in this step to our final clustering measurements.

4.2 Nearest neighbor redshift (NN) and Anderson et al. (2013) weighting schemes

An alternative fiber collision correction method is to simply assign a fiber-collided galaxy the redshift of its nearest neighbor (labelled NN in subsequent figures). In the limit of separations large compared to 62", this is equivalent to the method employed in our large-scale analyses, and described in detail in Anderson et al. (2013). In that work we assign the weight of a fiber collided galaxy to its nearest neighbor, which is propagated into the redshift distribution and correlation function calculations. A nice property of this method is that it is guaranteed to recover the correct large scale clustering amplitude of the full sample, at least in the limit of fiber collision *pairs* rather than groups. While the large scale bias is considered a nuisance parameter in galaxy auto-correlation analyses, it is used in cosmological parameter analyses when comparing galaxy clustering with galaxy-galaxy lensing, for example in the E_G test (Reyes 2010). This method will not recover accurate statistics on small scales, since the LOS separation between the collided and nearest neighbor galaxy will be artificially set to 0, thus suppressing true FOGs in the galaxy sample.

4.3 Solution using a tiled mock catalog

We generate a mock catalog covering the northern galactic cap portion of the SDSS-III BOSS survey using the LowRes simulation box listed in Table 1. The HOD parameters for this mock catalog were chosen based on a preliminary fit to preliminary measurements of ξ_ℓ: $M_{\min} = 8.62 \times 10^{12}\ h^{-1}\ M_\odot$, $M_1 = 2.16 \times 10^{14}\ h^{-1}\ M_\odot$, $M_{\mathrm{cut}} = -2.53 \times 10^{12}\ h^{-1}\ M_\odot$, $\sigma_{logM} = 0.43$, and $\alpha = 1.00$. The central galaxy velocities were defined using $\mathbf{v}_{\mathrm{COMV}}$, the center-of-mass velocity of the host halo. We also set $\gamma_{\mathrm{IHV}} = 1.27$ and $\gamma_{\mathrm{cenv}} = 0.48$ in order to get a reasonable fit to the observed clustering. All of these HOD parameters are described in detail in Sec. 6. In the following section we compare the clustering in the mock catalog with the data; the agreement is not perfect but sufficiently good for our purpose, which is to compare various fiber collision correction methods against the true clustering in the mock catalog.

We choose the number density of the HOD to be $\bar{n} = 4.2 \times 10^{-4}$ $(h^{-1}\ \mathrm{Mpc})^{-3}$, larger than the maximum value of the CMASS sample and first generate a uniform mock catalog using a single redshift output. We then apply the angular mask of the NGC for the final BOSS survey, and randomly downsample the mock galaxy catalog to match the observed CMASS $\bar{n}(z)$. We keep galaxies between $0.3 < z < 0.8$ in the mock catalog to account for the difference between the angular clustering of the full target sample and the angular clustering of the targets after applying the redshift cut $0.43 < z < 0.7$. Note that this mock catalog therefore meets the "constant clustering" assumption discussed in Sec. 4.1. This broader redshift coverage incorporates the vast majority of CMASS targets except for the 3% of targets that are stars. We make use of the approximate independence of the LOWZ and CMASS galaxy distributions, and input the positions of the true LOWZ and quasar targets before applying the BOSS tiling algorithm to the mock catalog. We measure the $w(\theta)$ for the full mock target sample and $w(\theta)$ for the mock target sample after applying redshift cuts, and find that on all scales of interest their ratio remains within 1% of 1.14, the value expected from Eq. 11. We also find that the angular weight that estimates w_s from the set of all targets assigned to fibers (and w_t corresponds to the full target sample) returns the same weight as our fiducial approach with redshift cuts, within 1%.

As we quantify in more detail in Sec. 5 and Fig. 8, our tiled mock catalog shows that the angular upweighting method recovers the true w_p within 1.5% on all scales, while the same is true above the fiber collision scale when using the nearest neighbor redshift method. Similarly for the $\hat{\xi}_{0,2}$ statistics, the nearest neighbor method almost perfectly recovers the true clustering above $s = 2$ h^{-1} Mpc. The angular method is nearly unbiased on scales below $s = 2\ h^{-1}$ Mpc, but shows systematic $\sim 2\sigma$ differences on intermediate scales for both $\hat{\xi}_2$ and ξ_2. Our final clustering estimators will use the nearest neighbor method on large scales and angular upweighting on small scales to infer the clustering of the CMASS sample in absence of fiber collisions, with systematic uncertainty below the statistical one. Therefore, we are not compelled to introduce any more complicated fiber collision correction schemes, such as the one recently proposed in Guo, Zehavi, & Zheng (2012). However, we note that their tests corroborate our findings that angular upweighting performs well on scales below the fiber collision scale, and the nearest neighbor method is unbiased on large scales. We note that their method has not yet been verified on a mock catalog with realistic tile-density correlations.
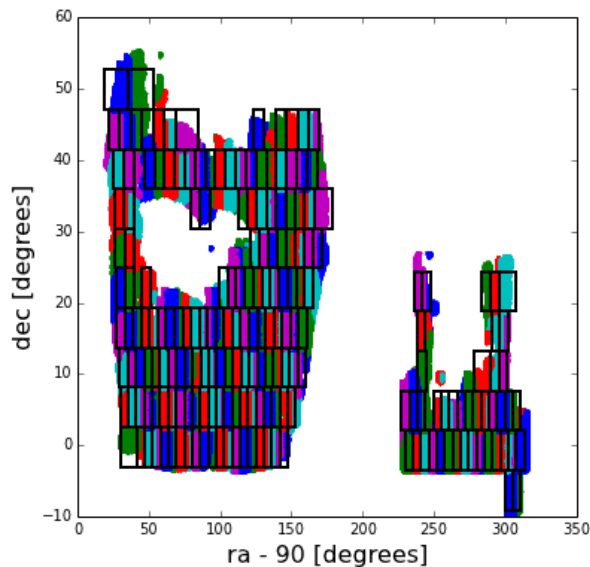
Figure 3. Two hundred bootstrap regions used to estimate the covariance matrix of observables from the survey. The individual subregions are squares (or a union of squares) in the coordinates Δdec, cos(dec)Δra.

5 MEASUREMENTS AND COVARIANCES

5.1 Survey Bootstrap Regions

We derive statistical covariances on our measurements by dividing the survey into 200 subregions, roughly equal in size and shape. Fig. 3 shows the regions. To define them, we first distributed square regions across the survey footprint with sidelength 5.56 degrees using Δdec, cos(dec)Δra coordinates. At $z = 0.57$ in our fiducial cosmology this corresponds to 145 h^{-1} Mpc on a side and the redshift extent from $z = 0.43$ to $z = 0.7$ translates to 608 h^{-1} Mpc. For comparison, the largest separations included in our ξ_ℓ measurements is 38 h^{-1} Mpc, and our w_p measurements extend along the LOS to 80 h^{-1} Mpc. Along each row of constant dec, we shifted the square centers in the ra direction to maximize the number of "nearly full" squares. We then grouped neighboring squares together in order to homogenize the number of galaxies per bootstrap region. Finally, galaxies and randoms outside any of the 200 bootstrap region were assigned to the nearest regions. The final distribution of randoms per bootstrap region had a one-σ scatter of $\sim 17\%$, accounting for both survey footprint incompleteness in the regions and variations in completeness for regions within the survey footprint. To derive bootstrap errors, we compute each observable separately in each subregion, excluding pairs that cross subregion boundaries. We use a single normalization between the data and random counts (though different for the north and south) that enters the Landy-Szalay estimator; this choice uses information from the entire survey to constrain the expected number density of galaxies as a function of redshift. The bootstrap covariance is then estimated as

$$C_{\mathrm{boot}} = \frac{1}{M-1} \sum_{k=1}^{M} (x_i^k - \bar{x}_i)(x_j^k - \bar{x}_j) \qquad (12)$$

and we set $M = 5000000$. Here x_i^k is the kth mean of N randomly selected (with replacement) x_i from the $N = 200$ subregion measurements.

Following Hartlap, Simon & Schneider (2007), we estimate the inverse covariance matrix as

$$\hat{C}^{-1} = \frac{n_{boot} - p - 2}{n_{boot} - 1} C_{boot}^{-1}; \quad (13)$$

but see discussions in Krause et al. (2013) and Eifler, Kilbinger, & Schneider (2008). In our case $n_{boot} = 200$, and $p = 27$ for our default analysis, which jointly fits $w_p(r_\sigma < 2\,h^{-1}\mathrm{Mpc})$ and $\hat{\xi}_{0,2}$. We verified that covariances derived by dividing the survey into a smaller number of boostrap regions (50 or 100) gave similar correlation structure, and diagonal errors reassuringly agreed at the $\sim 10\%$ level for w_p.

5.2 Angular clustering and fiber collision angular weights

The angular clustering of CMASS targets in the northern and southern galactic caps is shown in Fig. 4. A power law $w(\theta) = (\theta/39.75'')^{-0.99}$ is a reasonable description of the overall behavior, though $\sim 20\%$ level deviations are clearly detectable. We find $\chi^2 = 450$ for a power-law fit with 11 degrees of freedom. At $\sim 100''$ ($\sim 1\,h^{-1}$ Mpc), there is a dip that corresponds to the one-halo to two-halo transition region in the halo model. We find that the difference between the north and south measurements of $w(\theta)$ is consistent with our bootstrap errors, so there is no indication in this statistic that the galaxies in the two hemispheres we select cluster differently.

In this paper we analyze a single redshift-selected subsample of CMASS targets, $0.43 < z < 0.7$. 8% (9%) of targets in the north (south) are galaxies that fall outside this redshift range, with $p^2(\chi)$ in Eq. 10 of these discarded targets peaking in a relatively narrow range in χ near both redshift boundaries. Another 2.6% (3.1%) of targets are stars (neglected in the mock tiling), and their angular clustering is weak enough to be completely neglected on these scales. Following Hawkins et al. (2003) and White et al. (2011), we use Eq. 11 to relate the observed clustering of the full target sample (shown in Fig. 4) to the expected target clustering after the redshift cuts. We find $w_{t,subsample}/w_{t,full}$ is 1.18 (1.2) in the north (south) under the "constant clustering" assumption that targets inside and outside the redshift cuts have identical real-space clustering. If we instead assume that $\xi = 0$ outside our redshift cuts, this factor would be reduced by 6% (8%). Measurement of w_p for the galaxies outside our redshift cuts is noisy, but indicates that the constant clustering assumption is correct, within a factor of ~ 2. Therefore we assign a systematic uncertainty to w_t in Eq. 9 of 10%, shown as the grey bands in Fig. 5. Finally, unlike Hawkins et al. (2003), we do not systematically shift the angular coordinate of w_t in the full sample when estimating w_t for the redshift subsample; a $p^2(\chi)$ weighted mean of χ yields a difference of only 0.1% in the subsampled case. Our final estimates of the angular correction $w_{pair}(\theta)$ for the north (blue solid line) and south (green solid line) are shown in Fig. 5. The plate density in the south is slightly higher, so the angular weight is smaller than in the north on scales below the fiber collision radius. We also show the angular weight derived in the same manner using the tiled mock catalog (red). In the tiled mock catalog, the constant clustering assumption is accurate by construction. In all three cases, the weights quickly approach 1 above the fiber collision scale. For comparison, the dashed lines show angular weights derived setting w_s to the full sample of targets that were assigned fibers, and w_t to the full target sample, as opposed to our fiducial method of estimating both after applying redshift cuts. Within our 10% uncertainty in w_t, the two schemes are identical. We propagate the uncertainty in the angular
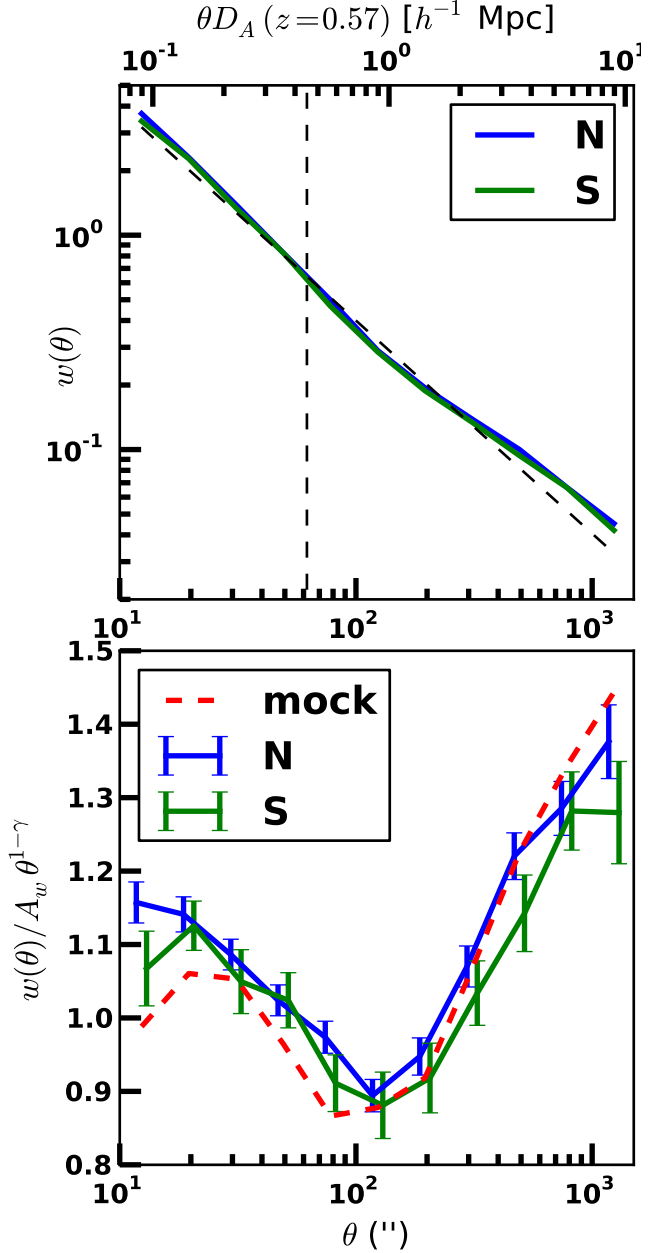

Figure 4. The clustering of CMASS targets in the north and south as a function of angular separation θ in arcseconds. The top axis translates angular scales to comoving separations at the effective redshift of our sample, $z_{eff} = 0.57$. The fiber collision scale, 62", is highlighted with the dashed vertical line in the upper panel. The dash-dot line shows the best fit power law. The lower panel highlights the $\sim 20\%$ deviation of the observed clustering from the best fit power law and also compares $w(\theta)$ measured in the northern and southern hemispheres to $w(\theta)$ for targets in tiled mock catalog (red). We show the diagonal elements of the bootstrap errors derived separately for the N and S, offset by ± 5 per-cent in θ for clarity.

pair weight by computing the statistics of interest (w_p, $\xi_{0,2}$, and $\hat{\xi}_{0,2}$) with our best estimate of w_{pair} as well as w_{pair} derived from $\pm 10\%$ changes in w_t in Eq. 9.
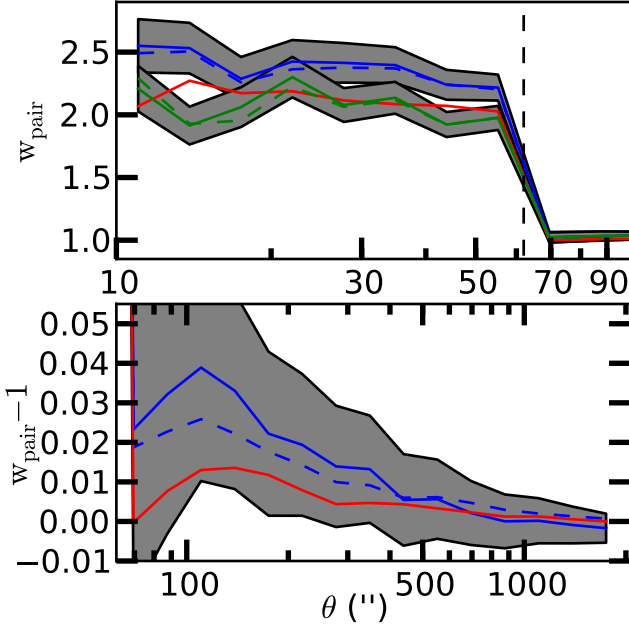
Figure 5. The angular weights as a function of pair separation (solid) in the North (blue) and South (green). The upper panel compares the w_{pair} below the fiber collision radius (dashed vertical line). The plate density in the south is slightly higher, so the angular weight is smaller on scales below the fiber collision radius. The red solid line is the angular weight derived from the tiled mock catalog. In the bottom panel, we show $w_{pair} - 1$ for the north (blue) and tiled mocks (red). The angular weight for the south is similar. For scales above the fiber collision radius, $|w_{pair} - 1|$ is smaller than 4% on all scales. To illustrate the level of correction to transform the full sample target clustering to the redshift cut subsample (i.e., w_t entering Eq. 9), we also show as dashed lines w_{pair} corresponding to w_s measured from all targets assigned fibers and w_t measured from the full target catalog. In this case star targets and galaxies outside our redshift cuts are included. These two schemes produce nearly identical angular weights. The grey bands indicate the uncertainty in w_t corresponding to the spectroscopic subsample that we propagate to our final estimates of w_p, $\hat{\xi}_{0,2}$, and $\xi_{0,2}$.

5.3 Projected correlation function w_p

In Fig. 6 we show our measurements of w_p in the northern (blue) and southern (green) hemispheres of the DR10 CMASS sample, compared with the tiled mock catalog (red). Errors on the south measurements are square root of the diagonal elements of the bootstrap covariance matrix after dividing by the fraction of total galaxies in the south. To assess the consistency of the two observations, we compute

$$\Delta_{NS} = (w_{p,N} - w_{p,S})_i C_{\text{boot},ij}^{-1} (w_{p,N} - w_{p,S})_j. \quad (14)$$

Assuming that the bootstrap covariance matrix can be rescaled using the total galaxy weight in the (independent) northern and southern subsamples to adequately describe the data covariances, we would expect

$$\langle \Delta_{NS} \rangle = \left(N_{\text{gal,S}} + N_{\text{gal,N}} \right) \left(N_{\text{gal,S}}^{-1} + N_{\text{gal,N}}^{-1} \right) n_{\text{bins}}, \quad (15)$$

where $N_{\text{gal,N}}$ ($N_{\text{gal,S}}$) are the total number of galaxies in our sample in the north (south). For w_p, $n_{\text{bins}} = 18$. We find $\Delta_{NS} = 110$ (expected 106) for the w_p estimated using nearest neighbor redshifts, and similar results for the angular upweighting method, so the two are perfectly consistent. We also compute Δ between the combined N+S w_p measurement and the tiled mock result; $\Delta = 136$ (91)
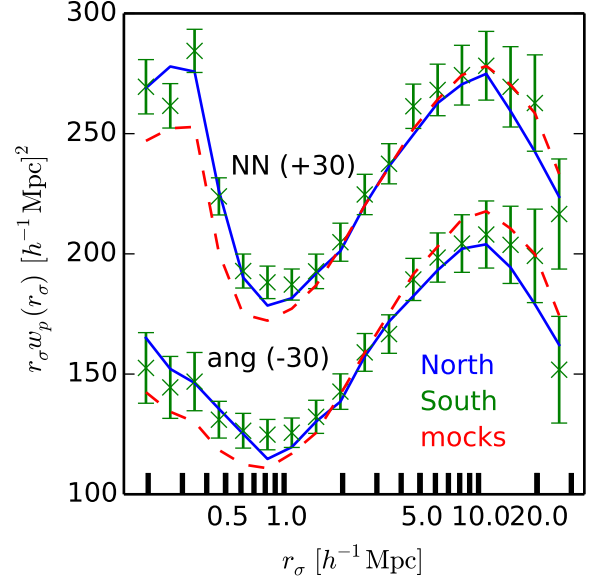

Figure 6. The projected correlation function $w_p(r_\sigma)$ in the north (blue), south (green), and tiled mock catalog (red). The upper curves use nearest neighbor ("NN") redshifts to correct for fiber collisions, while the lower ones use angular upweighting ("ang"); the curves have been offset in $r_\sigma w_p$ by ± 30 for visualization. On the south measurements, we show the square root of the diagonal elements of the bootstrap covariance matrix, multiplied by the inverse square root of the fraction of total galaxy weight in the south (i.e., a factor of 2 over the N+S bootstrap errors). The observed difference between the north and south are consistent with random realizations of the same underlying w_p. The mock catalog show fairly good agreement with the observations as well.

for the nearest neighbor and angular upweighting statistics, respectively, while we expect 73. The disagreement is worst in the nearest neighbor redshift case on the smallest scales, where we will adopt the angular upweighting result for our final analysis.

5.4 Anisotropic clustering measures $\hat{\xi}_\ell$ and ξ_ℓ

Fig. 7 shows a comparison of $\hat{\xi}_{0,2}$ measured from the north, south, and tiled mock catalog using the nearest neighbor redshift correction; results for angular upweighting and for $\xi_{0,2}$ are very similar. Applying Eq. 14 to $\hat{\xi}_{0,2}$ the disagreement between the north and south subsamples is larger: $\Delta_{NS} = 181$ (expected 106) but within the expected variation for this quantity. Comparing $\hat{\xi}_{0,2}$ from the tiled mock catalog to the data we find $\sim 2\sigma$ agreement for both angular upweighting and nearest neighbor redshift, which should be more than adequate for measuring the small differences between the true clustering and the clustering estimated from those correction methods.

5.5 Best estimators derived from tiled mocks and systematic uncertainties

As argued in Sec. 4.2, the nearest neighbor redshift assignment method ("NN") should provide nearly unbiased clustering estimates on large scales, as long as one avoids small r_σ contributions, so we will rely on this method on scales well above the fiber collision scale. On smaller scales angular upweighting ("ang") method
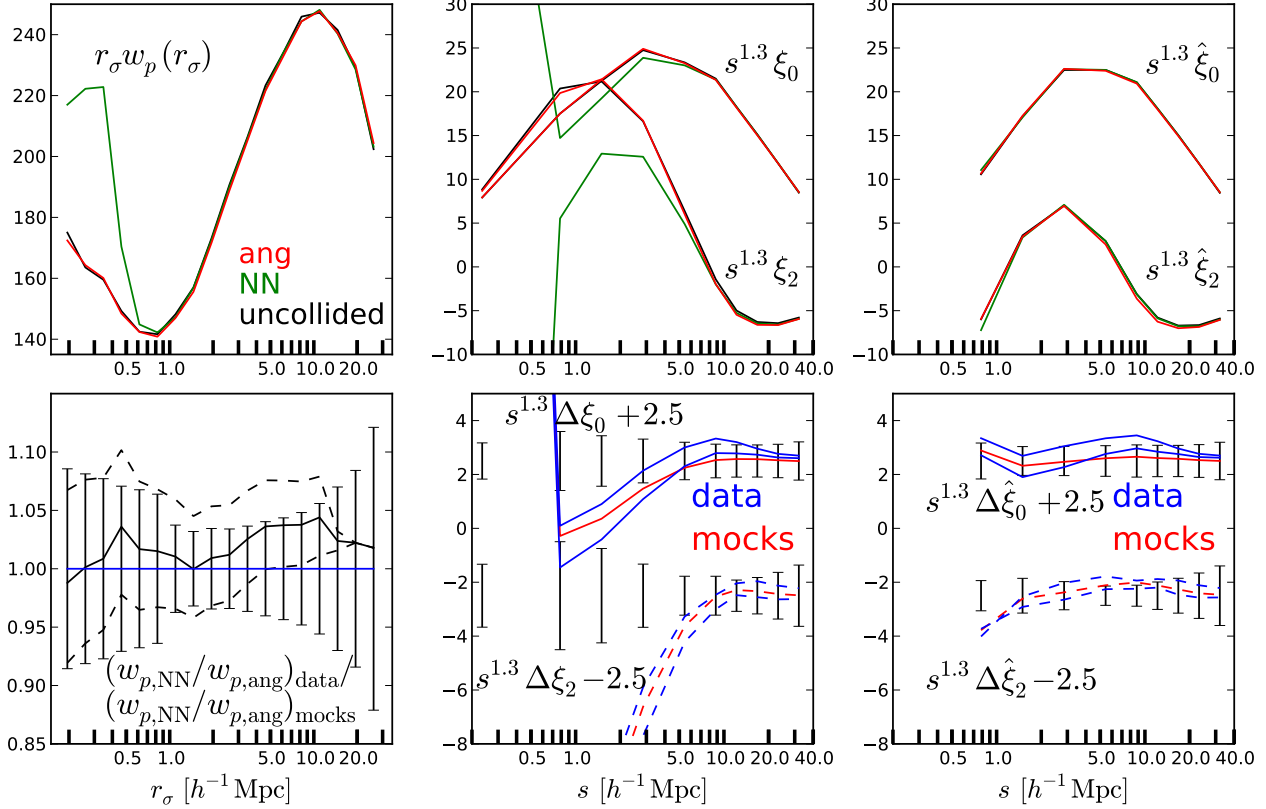
Figure 8. Fiber collision correction validation. In the top three panels we show w_p, $\xi_{0,2}$, and $\hat{\xi}_{0,2}$ as measured from our tiled mock catalog in the absence of fiber collisions ("uncollided"; black), using the angular upweighting method ("ang"; red), and using the nearest neighbor redshift method ("NN",green). The angular upweighting method is quite accurate on all scales, but subject to additional uncertainties for the data; we use that method on small scales and transition to the nearest neighbor redshift method on large scales, which we expect to be very close to unbiased. The bottom panels compare the difference between the angular upweighting and nearest neighbor redshift methods measured from both the data and the mocks, allowing us to demonstrate consistency between the data and mock galaxy catalogs. For w_p we show this comparison as a ratio (black) along with its uncertainty from the uncertainty in the angular weights (dashed lines). In the middle and right bottom panels, the blue curves bracket the measured difference between the angular upweighting and nearest neighbor estimators for each of the four statistics $s^{1.3}\xi_{0,2}$ and $s^{1.3}\hat{\xi}_{0,2}$. The distance between the two blue curves for each statistic originates from the uncertainty in deriving the angular weights for the data. The red curves show the same differences measured from the mocks. In all three panels we also show diagonal errors from our final measurements + theory total covariance matrix presented in Sec. 5.6. We find good agreement between the data and mocks in all three panels, lending support to our final fiber collision correction methodology.

is more accurate. In Fig. 8 we compare the underlying "uncollided", complete target catalog (black) with the nearest neighbor redshift (green) and angular upweighting (red) methods for recovering the underlying clustering. In this figure we investigate the three statistics of interest, w_p, $\xi_{0,2}$, and $\hat{\xi}_{0,2}$. On small angular scales the angular upweighting method does indeed recover the underlying clustering at high accuracy for all three statistics, while the nearest neighbor method is effective only on larger scales. The comparison between the middle and right panels illustrates the large contribution of the scales $r_\sigma/D_A(z) < 62''$ to the multipoles $\xi_{0,2}$. Eliminating those scales brings the nearest neighbor and angular upweighting estimators into very good agreement for the $\hat{\xi}_{0,2}$ statistic, which is why we choose to include it rather than $\xi_{0,2}$ in our parameter fitting. With this comparison in hand, we define our best estimate of these statistics from the data in the following way. For each statistic (w_p, ξ_0, ξ_2, $\hat{\xi}_0$, $\hat{\xi}_2$), we use the difference between the two estimators and the "truth" to determine a transition scale at which we switch from the angular estimator on small scales to the nearest neighbor redshift estimator on large scales; we find $(1.09, 8.8, 12.2, 1.5, 1.5)\, h^{-1}$ Mpc. Next, we use the difference between the estimator and "truth"

in the mock catalogs as an estimate of the bias of the observed statistics. We subtract this difference from our measurements, and add its square to the diagonal elements of the bootstrap covariance matrix. For w_p this correction is completely negligible. For $\hat{\xi}$ it is $< 0.3\sigma$ except for $\hat{\xi}_2(1.5\, h^{-1}\mathrm{Mpc})$, for which the shift is 0.7σ; here σ refers to the diagonal element of the bootstrap covariance matrix. This difference is slightly larger than 1σ for ξ_2 in the range 5.4-12.2 h^{-1} Mpc. For points using the angular upweighting method, we translate the $\pm 10\%$ uncertainty in the angular weights, shown in Fig. 5, into an additional uncertainty on the measured statistics. We add this source of uncertainty to the diagonal of the bootstrap covariance matrices, which were computed using fixed angular pair weights. This increases the diagonal uncertainty on the clustering by a factor of two or more for the points affected. The resulting estimate of $w_p(r_\sigma)$ as well as the diagonal uncertainty is tabulated in Table 2, and $\hat{\xi}_{0,2}$ and $\xi_{0,2}$ are listed in Table 3.

In the lower set of plots in Fig. 8, we compare differences in all three statistics using the nearest neighbor redshift and angular upweighting method measured in both the mocks and the data; for comparison, we show diagonal uncertainties from our final covari-
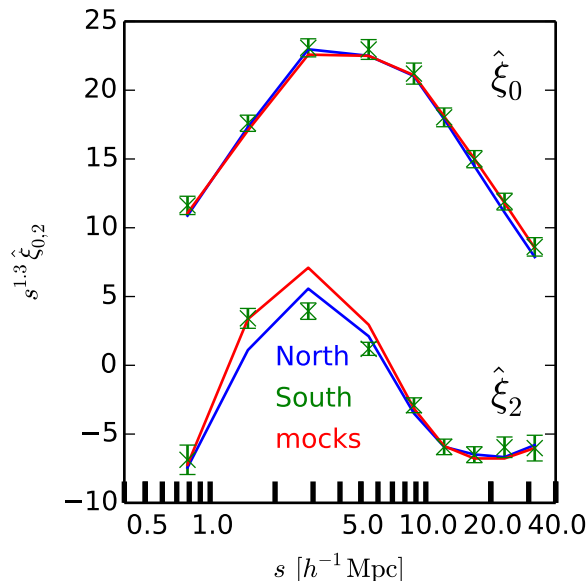
5.6 Combined measurement and theory covariance matrix

So far we have accounted for three sources of uncertainty in our measurements: the standard finite volume sampling, for which we estimate a full measurement covariance matrix using the 200 bootstrap regions in Fig. 3; 10% uncertainty in the angular weights used in the angular upweighting method, which we propagate to the observables of interest and then add to the diagonal elements of the covariance matrix; and systematic uncertainty equal to the size of debiasing correction derived from the mock tiling catalog and added to the diagonal elements of the covariance matrix. The combination of these three terms we call our "measurement" uncertainty. One final source of statistical error comes from uncertainty in our theoretical prediction. The total volume within the DR10 survey mask after applying our redshift cuts is ~ 2.5 $(h^{-1}$ Gpc$)^3$, though some of this volume is mapped with a low number density of galaxies. The HiRes N-body simulation box, for which we estimate the theoretical error, covers only $\sim 1/8$ of that volume. Our theoretical calculation averages over all possible realizations of a particlar HOD (for the given halo catalog), which removes much of the sampling variance from the theoretical calculation. Cosmic variance assoicated with the underlying dark matter realization remains, but the theoretical error will be smaller than the naive volume comparison suggests.

In order to estimate the theoretical uncertainty, we populate the LowRes simulation halo catalogs with the same HOD as in Sec. 4.3. We divide the box into 4^3 subboxes the size of the HiRes box, which allows for a 10 h^{-1} Mpc buffer between subboxes in each direction. We again include the factor in Eq. 13 with $n_{\rm boot} = 64$ to unbias the inverse bootstrap covariance matrix estimate; for $n_{\rm bin} = 27$, the prefactor is 1.8. More simulation volume could reduce both the theoretical uncertainties and covariance, but is only justified if we have not reached a systematics floor in the theoretical modeling. The left panel of Fig. 9 compares the diagonal elements of the final "measurement" uncertainties with the theoretical uncertainties. We sum the measurement and theory covariance matrices to arrive at our final covariance matrix that we will invert and use in a standard χ^2 analysis to do model parameter fitting. In the right panel, we show the correlation matrix for the $C_{\rm tot} = C_{\rm meas} + C_{\rm theory}$. As is true on large scales as well, neigboring bins in $\hat{\xi}_0$ are highly correlated, meaning the data is relatively insensitive to overall changes in the amplitude of clustering, but more sensitive to spatially-abrupt model signatures (like the BAO feature). The $\hat{\xi}_2$ bins are less correlated than $\hat{\xi}_0$ for large separations, and there is significant covariance between all three observables. At large separations, $\hat{\xi}_2$ becomes negative, so a positive correlation in the amplitude of the multipoles (as we would expect from uncertainty in an overall bias factor) shows up in that region as an anti-correlation.

6 MODEL

The only detailed semi-analytic HOD based descriptions of galaxy clustering in redshift space available to our knowledge are given in Tinker (2007) and Zu & Weinberg (2012). The models presented therein require a description of the probability distribution of pairwise halo line-of-sight velocities as a function of their real space separation, orientation with respect to the line of sight, and the two halo masses. These distributions have substantial skewness and kurtosis that depends on pair separation and halo masses. These semi-analytic models require calibration of several scaling relations

Figure 7. The pseudo-multipoles $\hat{\xi}_{0,2}$ defined in Eq. 7 measured from the north (blue), south (green) and mock tiling catalog (red), as in Fig. 6 using nearest neighbor redshifts to correct for fiber collisions.

r_σ	w_p	σ_{w_p}	r_σ	w_p	σ_{w_p}
0.195	**1000.5**	85.6	2.60	73.8	2.5
0.260	**691.7**	56.2	3.46	59.8	2.2
0.346	**507.7**	39.2	4.62	48.4	2.0
0.462	**358.1**	25.3	6.16	38.0	1.7
0.616	**252.4**	17.1	8.22	29.6	1.4
0.822	**179.8**	11.5	10.96	22.3	1.2
1.096	140.3	5.2	14.61	15.9	1.1
1.461	111.0	3.5	19.48	11.2	0.9
1.948	88.5	3.1	25.98	7.4	0.9

Table 2. Fiber collision corrected measurements of the projected correlation function $w_p(r_\sigma)$ for $\pi_{\rm max} = 80$ h^{-1} Mpc defined in Eq. 5. The first 9 bins ($r_\sigma < 2$ h^{-1} Mpc; left half of the table) are included in joint fits with $\hat{\xi}_{0,2}$. The bolded w_p values are derived using the angular upweighting method while the rest use the nearest neighbor redshift method.

ance matrix presented in Sec. 5.6. Differences between these two observables are determined by the redshift distribution and clustering properties of the galaxy sample as well as the tiling algorithm. These differences seen in the data are reproduced with good accuracy by our mock catalogs.

In the left panel we compare the ratio of $w_{p,\rm NN}/w_{p,\rm ang}$, which is large below the fiber collision scale and approaches 1 on large scales in the mocks. The data behaves similarly, but with a relatively constant factor ~ 1.02 offset with the mocks. This offset is within the reported angular upweighting uncertainty (dashed curves) and also small compared to our final error budget. In the middle and right bottom panels we show instead the difference $s^{1.3}(\xi_{\ell,\rm NN} - \xi_{\ell,\rm ang})$; the same offset in w_p is also present in ξ_0 and $\hat{\xi}_0$. The blue curves in these panels show the allowed region after propagating our 10% uncertainty in the angular weights, and the red curves show the differences measured from the mock catalogs. They are consistent within the uncertainties.

s_{cen}	s_{low}	s_{high}	$\mu_{max,low}$	$\mu_{max,high}$	ξ_0	σ_{ξ_0}	$\hat{\xi}_0$	$\sigma_{\hat{\xi}_0}$	ξ_2	σ_{ξ_2}	$\hat{\xi}_2$	$\sigma_{\hat{\xi}_2}$
0.234	0.097	0.569	0.000	0.000	**57.757**	4.428	-	-	**60.471**	7.699	-	-
0.785	0.569	1.084	0.345	0.845	**24.665**	1.497	**14.339**	0.913	**30.726**	2.744	**-8.346**	0.767
1.496	1.084	2.065	0.870	0.955	**12.841**	0.555	10.363	0.317	**11.687**	1.037	1.094	0.382
2.851	2.065	3.936	0.965	0.985	**6.403**	0.208	5.865	0.139	**3.811**	0.300	1.309	0.134
5.433	3.936	7.499	0.990	0.995	**2.559**	0.077	2.503	0.063	**0.633**	0.080	0.212	0.040
8.810	7.499	10.351	0.995	0.995	1.273	0.037	1.244	0.035	**-0.074**	0.043	-0.197	0.023
12.162	10.351	14.289	0.995	0.995	0.707	0.023	0.696	0.023	-0.185	0.023	-0.227	0.020
16.788	14.289	19.724	0.995	0.995	0.377	0.015	0.374	0.015	-0.151	0.017	-0.164	0.017
23.174	19.724	27.227	0.995	0.995	0.190	0.010	0.189	0.010	-0.103	0.015	-0.107	0.014
31.989	27.227	37.584	0.995	0.995	0.088	0.008	0.088	0.008	-0.062	0.013	-0.063	0.012

Table 3. Fiber collision corrected measurements of $\xi_{0,2}$ and $\hat{\xi}_{0,2}$. The first column is the logarithmic bin center used in all plots. The minimum and maximum redshift space separations in each bin are listed as s_{low} and s_{high}, and the corresponding maximum μ_{max} for $\hat{\xi}_{0,2}$ (see Eq. 7) are listed as $\mu_{max,low}$ and $\mu_{max,high}$ (recall μ_{max} is allowed to vary with s). We use $r_\sigma < 0.534\ h^{-1}$ Mpc to define μ_{max}, which corresponds to 62" at $z = 0.7$ in the cosmology with $\Omega_m = 0.274$ used to compute comoving pair separations. For $\xi_{0,2}$, $\mu_{max} = 1$ for all s bins. The latter columns show our fiber-collision corrected estimates of $\xi_{0,2}$ and $\hat{\xi}_{0,2}$ defined in Eq. 6 and 7 as well as the diagonal elements of the total (measurements + theory) covariance matrix. The bolded $\xi_{0,2}$ and $\hat{\xi}_{0,2}$ values are derived using the angular upweighting method while the rest use the nearest neighbor redshift method.
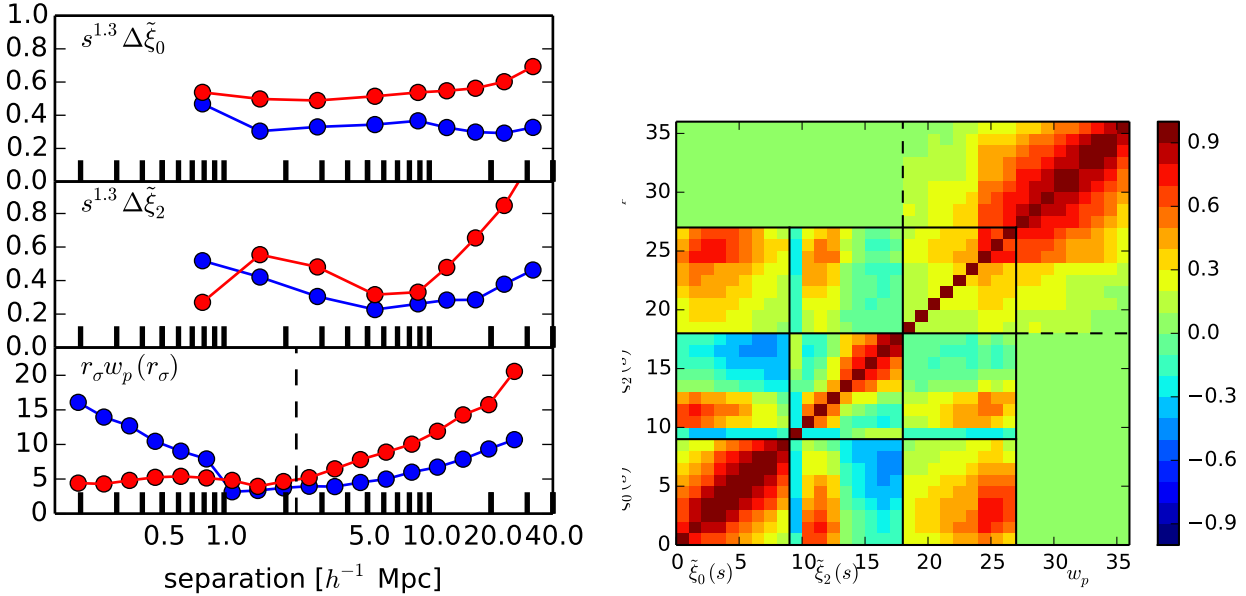

Figure 9. *Left panel:* The diagonal elements of the measurement covariance matrix (blue) and the theory covariance matrix (red). On small scales measurement errors are large due to the 10% uncertainty in the angular weights used in the angular upweighting method for fiber collision corrections. Theory errors are due to our use of an N-body simulation box smaller than the observational volume and dominate the error budget on most scales. Only measurements of w_p below the dashed line are included in our joint fits to $\hat{\xi}_{0,2}+w_p$. *Right panel:* The reduced total covariance matrix for $\hat{\xi}_{0,2}+w_p$ (first 27 elements). We also show the full w_p covariance out to larger scales, though those data points are not included in the joint fits. Off-diagonal elements between $\hat{\xi}_{0,2}$ and large scale w_p are artificially set to 0 in this plot. We overlay black lines that divide the $\hat{\xi}_0$, $\hat{\xi}_2$, and w_p sections of the covariance matrix into three blocks of nine measurements each. Only these points are used to fit the parameters of the model.

against N-body simulations; fine-tuning or extending it to reach the precision demanded by our measurements would likely be extremely challenging.

Throughout the present analysis we therefore resort to deriving our theoretical predictions directly from mock galaxy catalogs based on N-body simulations, as detailed below. The disadvantage of this approach is that cosmological parameter dependences are not easily incorporated, and the theory evaluation must be fast enough to permit at least a five-dimensional Monte-Carlo HOD parameter exploration. Following Neistein & Khochfar (2012) we implemented a pre-calculation of pair counts in fine mass bins; sums over these counts allow fast evaluation of the theoretical prediction as a function of HOD parameters. However, parameters that alter

the velocity of galaxies change all pair separations and therefore require recalculation of the pair counts. We explored interpolation of the pair counts across the set of three velocity parameters described in Sec. 6.3. While useful for determining parameter degeneracies and expected uncertainties, the resulting constraints were not sufficiently accurate given the coarseness of the velocity parameter sampling. We therefore resort to varying one or at most two velocity parameters simultaneously.

6.1 Halo and central velocities

For a given SO halo catalog, we consider two definitions of halo velocities; these velocities are assigned directly to "central" galaxies,
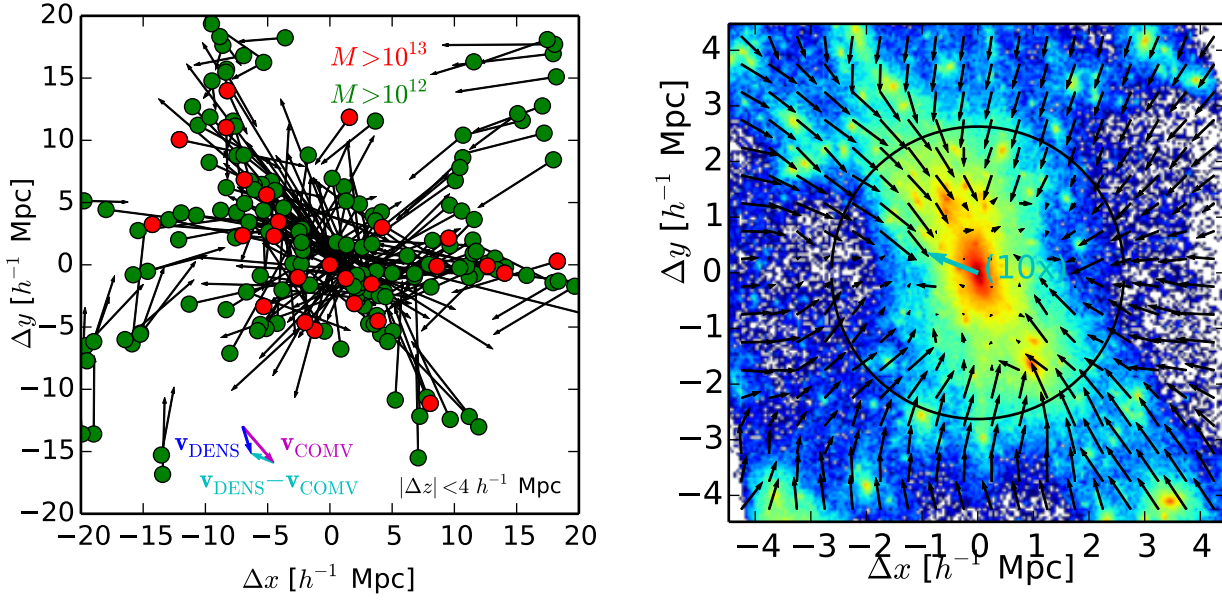
Figure 11. *Left:* A $|\Delta z| < 4\, h^{-1}$ Mpc slice through the HiRes simulation box, centered on the largest halo in the box with $M = 1.3 \times 10^{15}\, h^{-1} M_\odot$. Green (red) dots indicate the positions of halos of mass $M > 10^{12}\, (10^{13})\, h^{-1} M_\odot$, where all positions have been projected into the plane determined by the vectors $\mathbf{v}_{\mathrm{DENS}}$ (blue) and $\mathbf{v}_{\mathrm{COMV}}$ (magenta). The black arrows indicate the velocity of each halo (in distance units) relative to $\mathbf{v}_{\mathrm{COMV}}$, so that the central halo center of mass is at rest. *Right:* A zoomed-in version of the left panel with the log of the matter density over-plotted along with the central halo virial radius $r_{\mathrm{vir}} = 2.7\, h^{-1}$ Mpc. The matter velocity field is over-plotted in black alongside the halos; the velocity vectors in this panel were scaled down by a factor of 20 for visualization purposes. The central cyan vector shows $\mathbf{v}_{\mathrm{DENS}} - \mathbf{v}_{\mathrm{COMV}}$, scaled down by a factor of only two (so expanded by a factor of 10 compared to the other vectors). The inward flow from the upper left corner pushes $\mathbf{v}_{\mathrm{COMV}}$ along the $+\hat{e}_x$ compared with $\mathbf{v}_{\mathrm{DENS}}$. The clear correlation between the density field and central galaxy velocity will be imprinted differently on $\hat{\xi}_{0,2}$ than if $\mathbf{v}_{\mathrm{DENS}}$ - $\mathbf{v}_{\mathrm{COMV}}$ were randomly oriented.
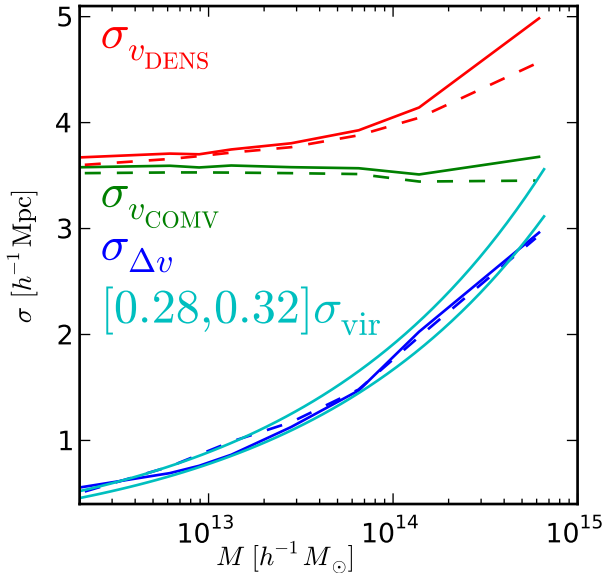

Figure 10. The rms velocities as a function of halo mass for the two central velocity definitions ("DENS" in red and "COMV" in green), as well as their difference (blue). Solid lines are derived from the HiRes simulation while dashed lines are from the MedRes simulation. The difference between those vectors has a magnitude consistent with $[0.3 \pm 0.02]\sigma_{\mathrm{vir}}$, shown by the cyan curves.

and the intrahalo velocity component for satellite galaxies is defined with respect to this halo velocity. The first choice is to simply average the velocities of all the halo members, denoted $\mathbf{v}_{\mathrm{COMV}}$, for center-of-mass velocity. The dispersion of halo member velocities around the center-of-mass velocity is

$$\sigma_{\mathrm{vir}} = 2.79 h^{-1}\,\mathrm{Mpc} \left(\frac{M}{10^{13} h^{-1} M_\odot} \right)^{0.331}, \qquad (16)$$

fit to halos in the HiRes box; the HiRes and MedRes dispersions agree within 2% with this relation, the LowRes box within 5%. The three are in per-cent level agreement above $10^{14} h^{-1} M_\odot$. Therefore, within the range accessible to this study, the intrahalo velocity dispersions are independent of both cosmology and simulation resolution within a few per-cent, at fixed SO halo mass. The green curves in Fig. 10 show that the rms center-of-mass halo velocity σ_{COMV} is remarkably independent of halo mass (within 2% of 3.57 h^{-1} Mpc for $10^{12-15} h^{-1} M_\odot$ halos in the HiRes box). The MedRes σ_{COMV} is lower by a factor of 1.016, in reasonable agreement with the linear theory expectation of 1.021 given the ratio of the values of $f\sigma_8$ for the two boxes.

The second central velocity definition, $\mathbf{v}_{\mathrm{DENS}}$, was defined precisely in Sec. 2.4, and the sensitivity to this definition was explored in more detail in Appendix B. Note that in both catalogs we use that same density peak to define the halo center, where we place the "central" galaxy, so positions in the two halo catalogs we compare are identical; only the "central" galaxy velocities are different. Fig. 10 shows that the magnitude of $\mathbf{v}_{\mathrm{DENS}}$ rises with halo mass. If we consider the difference vector $\mathbf{v}_{\mathrm{COMV}} - \mathbf{v}_{\mathrm{DENS}}$, we get the blue curves in Fig. 10. We see that $|\mathbf{v}_{\mathrm{COMV}} - \mathbf{v}_{\mathrm{DENS}}|$ depends on mass in

the same way as the halo virial velocity (Eq. 16), but the magnitude is smaller by a factor of 0.3.

Fig. 11 illustrates these velocity vectors in the local environment of the largest halo in the HiRes simulation, which has $M_{\rm halo} = 1.3 \times 10^{15}\, h^{-1} M_\odot$. The real space coordinates have been shifted to place the halo at the (0,0) and projected into the plane defined by $\mathbf{v_{DENS}}$ (blue) and $\mathbf{v_{COMV}}$ (magenta). In the left panel we take a $|\Delta z| < 4\, h^{-1}$ Mpc slice around the central halo and plot the positions (dots) and velocities (relative to $\mathbf{v_{COMV}}$ of the central halo; black vectors) of halos within $\pm 20\, h^{-1}$ Mpc in Δx and Δy. The relative velocity of the dense clump of the central halo is shown as the cyan vector. In the right panel we examine the virial region (marked by the black circle) and surrounding structure with a log mapping of the density field. Mean matter velocities are shown with black arrows, scaled down by a factor of 20 for visualisation purposes. The net offset $\mathbf{v_{DENS}} - \mathbf{v_{COMV}}$ is shown as the cyan vector, scaled down only by a factor of two; it is inherently much smaller than the infall region velocities, and is correlated with a major filamentary structure. The correlation will be imprinted in $\hat{\xi}_{0,2}$ since the relative velocity will preferentially move pairs along the filamentary structure and thus preferentially along their separation vector.

One final point of interest in comparing these vectors is that the difference vector contains a component along the $\mathbf{v_{COMV}}$ direction, such that the magnitude of $\mathbf{v_{DENS}}$ is larger in that direction by 1.5%. This provides a ballpark upper limit on how much the central galaxy velocity details may alter the effective $f\sigma_8$ on large scales, if the correlation is sourced by the quasilinear velocity component driving the large-scale Kaiser distortions. We propagate these two velocity choices to galaxy clustering predictions in Sec. 7.2. Further investigation is warranted beyond these two choices. However, given the good agreement between our "central" velocity definition and the more detailed phase-space investigation given in Behroozi, Wechsler, & Wu (2013), we assert that $\mathbf{v_{DENS}}$ is the more physical choice of the two.

6.2 Number Density Prior and Redshift Evolution

Our HOD model based on a fixed redshift N-body simulation halo catalog can only be an approximation to the real CMASS galaxy sample, for which the number density $\bar{n}(z)$ varies considerably across the redshift range of our sample; potentially the galaxy properties are redshift dependent as well (see earlier work on this topic in Masters et al. 2011; Ross et al. 2012, 2014). Remarkably, in Appendix A we find that there is no measurable redshift evolution in the $\hat{\xi}_{0,2}$ statistic across the sample, even though the number density drops by a factor of 2.2 in the high redshift sample. We therefore take the simple ansatz that galaxies at all redshifts are a random subsample drawn from a single population. The observed $\bar{n}(z)$ simply reflects the fraction of the parent population selected by the CMASS targeting algorithm as a function of redshift. While a more complete model would allow all the HOD parameters to vary with redshift to match the observed $\bar{n}(z)$, the data do not require it and it cannot be done without considerably increasing the complexity of our theoretical calculation (i.e., requiring the generation of lightcone halo catalogs).

Fig. 12 shows the cumulative probability distribution of $\bar{n}(z)$ at the redshift of the galaxies in CMASS after applying the redshift cut $0.43 < z < 0.7$. The vertical lines show the hard prior we assumed when fitting the single underlying HOD, $3.25 < 10^4 \bar{n}_{\rm HOD} < 4.25$ in units of $(h^{-1}$ Mpc$)^{-3}$. The lower bound is set by requiring the parent population to have higher number density than the typical CMASS galaxy. The upper bound depends on the completeness
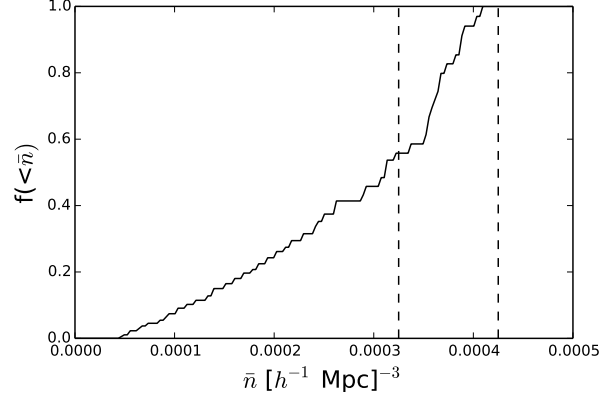

Figure 12. Cumulative distribution of $\bar{n}$ for the CMASS sample with redshift cut $0.43 < z < 0.7$. The vertical dashed line shows the fiducial hard prior adopted when fitting HOD models, $3.25 < 10^4 \bar{n}_{\rm HOD} < 4.25$ in units of $(h^{-1}$ Mpc$)^{-3}$.

of our target selection, which in turn depends on the size of the photometric uncertainties in the imaging data. We have chosen a value safely above the peak of the number density distribution for the fiducial case, and will demonstrate in Sec. 7.6 that our constraints on $f\sigma_8$ are insensitive to this choice. As discussed in Sec. 7.6, the observed galaxy clustering amplitude and the abundance of sufficiently highly biased halos sets a hard upper limit of $\approx 6 \times 10^{-4}$ $(h^{-1}$ Mpc$)^{-3}$.

6.3 Halo Occupation Distribution (HOD) parameters and implementation

The parametrisation of the HOD we adopt follows Zheng et al. (2005), and has been used in a number of studies focusing on the SDSS-II Luminous Red Galaxy sample (Reid & Spergel 2009), the SDSS-III CMASS sample (White et al. 2011), and the SDSS-III LOWZ sample (Parejko et al. 2013). We separately model central and satellite galaxies, assuming that a central galaxy is required for a given halo to host a satellite galaxy. We model the probability for a halo of mass M to host a central galaxy as

$$N_{\rm cen}(M) = 0.5 \left[1 + {\rm erf}\left(\frac{\log_{10} M - \log_{10} M_{\rm min}}{\sigma_{\log_{10} M}} \right) \right]. \qquad (17)$$

In our default model, the central galaxy is assigned to the position and velocity ($\mathbf{v_{DENS}}$) of the density peak of its host dark matter halo. We also test a model with the same position assignment, but set the central velocity to $\mathbf{v_{COMV}}$. Given that a given halo of mass M hosts a central galaxy, the number of satellites assigned to the halo is drawn from a Poisson distribution with mean

$$N_{\rm sat}(M) = \left(\frac{M - M_{\rm cut}}{M_1} \right)^\alpha. \qquad (18)$$

We set $N_{\rm sat}(M < M_{\rm cut}) = 0$. The average total number of galaxies in a halo of mass M is then

$$\left\langle N_{\rm gal}(M) \right\rangle = N_{\rm cen}(M) \left(1 + N_{\rm sat}(M) \right). \qquad (19)$$

For each satellite galaxy we assign the position and velocity of a randomly chosen dark matter particle member of the host halo. When fitting for the HOD parameters we sample $\log_{10} M_{\rm min}$, $\log_{10} M_1$, and $\log_{10} M_{\rm cut}$ so all masses are constrained to be larger than 0.
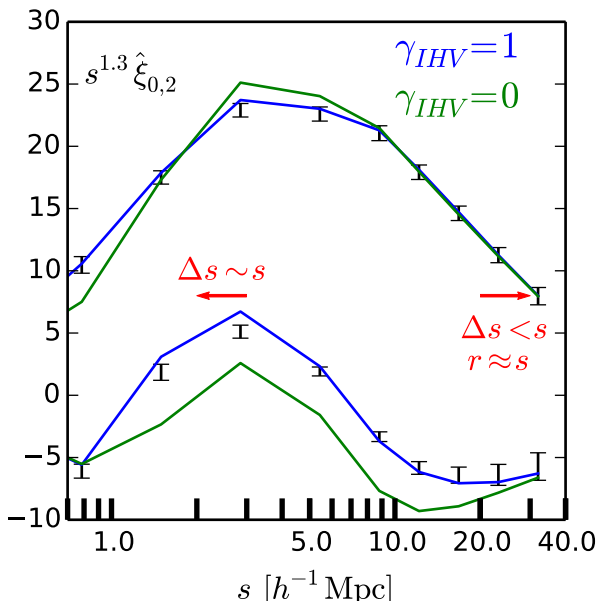
Figure 13. Best fit model to the MedRes simulation for $\gamma_{HV} = 1$, $\gamma_{IHV} = 1$, $\gamma_{cenv} = 0$ (blue) compared with the same HOD model but with the satellite velocities artificially set to 0 ($\gamma_{IHV} = 0$; green) and their positions set to the position of the central galaxy. The satellite velocity dispersion distorts $\hat{\xi}_0$ only below 10 h^{-1} Mpc. Removing the satellite intrahalo velocities lowers the quadrupole significantly on all scales of interest. For separations of $\sim$ 3 h^{-1} Mpc and below, the difference between true and apparent (redshift space) separations is comparable or larger than s and sets the scale of the transition from positive to negative for the $\gamma_{IHV} = 0$ model. On larger scales, true and apparent separations are similar, since Δs is small compared to s. For comparison our measurements are shown with black error bars.

We also introduce three new parameters that rescale the galaxy velocities without altering their positions.

- γ_{HV}: This parameter rescales all halo velocities in the simulation. If linear theory were accurate on all scales, a fractional change in γ_{HV} would be equivalent to a fractional change in the large-scale peculiar velocity field amplitude, $f\sigma_8$. In Sec. 7.7 we demonstrate the validity of this approximation for relative halo velocities even on non-linear scales. Our constraints on γ_{HV} are derived by interpolating across the theoretical model evaluated between $\gamma_{HV} = 0.9 - 1.1$ in steps of 0.01. For our fiducial fit, the lower bound is $\sim 2.5\sigma$ away from the best fit.
- γ_{IHV}: This parameter rescales the velocity of satellite galaxies relative to the host halo. Conceptually, this amounts to rescaling the virial velocity of the halo and/or accounting for sub-halo/galaxy velocity bias effects.
- γ_{cenv}: This parameter specifies an additional random (Gaussian) dispersion for central galaxies in units of the halo virial velocity.

6.4 Interpreting $\hat{\xi}_{0,2}$ in the halo model

One prime advantage of the w_p observable is that the x-axis (projected separation r_σ) draws a neat separation between the two physical components of the halo model; the majority of pairs with r_σ smaller than the virial radius of the typical host halo actually occupy the same host halo (the "one-halo" term); on larger scales, pairs originate from different host halos (the "two-halo" term).

Such a distinction is impossible at small redshift space separations s. Although an extreme example, Fig. 11 illustrates the large intrahalo velocities on small scales, and how they blur the underlying small-scale structure. Using the results of Reid & White (2011), we find that halos of mass $\sim 10^{13.1}$ h^{-1} $M_\odot$ have a mean relative pairwise velocity of ~ -2.7 h^{-1} Mpc at separations below 10 h^{-1} Mpc and a pairwise velocity dispersion that increases with scale, also with an rms of ~ 2.7 h^{-1} Mpc at true (real space) halo separations of 5 h^{-1} Mpc. Thus we expect that below scales of ~ 3 h^{-1} Mpc, there is little correlation between the observed redshift pair separation s and the true one; as shown in Fig. 13, this is the scale where $\hat{\xi}_2$ transitions from positive to negative for the underlying halo distribution (see the green $\gamma_{IHV} = 0$ model curve where satellite velocities have artificially been set to 0).

Fig. 13 also shows that there is a plethora of information in $\hat{\xi}_2$ on the satellite galaxy velocity dispersion. The satellite velocity dispersion distorts $\hat{\xi}_0$ only below 10 h^{-1} Mpc. Removing the satellite intrahalo velocities lowers the quadrupole significantly on all scales of interest. The χ^2 difference between an HOD model fit to the data and the same model without satellite velocity distpersions is 400.

7 RESULTS

In this section we fit the measured w_p and $\hat{\xi}_{0,2}$ using the covariance matrix presented in Sec. 5.6 and Fig. 9 to the model described in Sec. 6. Our recommended constraints based on our best guesses regarding modeling choices (justified further below) are indicated in Table 4 as the bold "fiducial" column, while many other modeling choices are presented there only for comparison. We also indicate parameters held fixed in particular analyses by bold.

7.1 Choice of measurement combination w_p and $\hat{\xi}_{0,2}$

In this analysis we study galaxy clustering on scales below the typical host halo virial radius, out to the quasi-linear scales used in our large-scale RSD measurements. The maximum scale included sets a limitation on the number of available bootstrap regions from the survey, and that, in turn, sets a limit on the number of observables for which we can reliably estimate a covariance matrix. It was thus our goal to determine a minimal set of observables that contained most of the available clustering information on the scales of interest. Initially we considered fits only to either $\xi_{0,2}$ or $\hat{\xi}_{0,2}$. We prefer the latter because of its insensitivity to fiber collision corrections and smaller uncertainties. We found that these two observables preferred distinct regions of HOD parameter space, at least in our fiducial HOD parametrization: fits to $\hat{\xi}_{0,2}$ alone prefer a low satellite fraction of 6.5% and did provide a better fit to the small-scale behavior of $\hat{\xi}_{0,2}$ than presented below. However, this model was in strong tension with both w_p and $\xi_{0,2}$ on small scales because of the low satellite fraction. We concluded that information relevant to the satellite HOD parameters was missing from $\hat{\xi}_{0,2}$, and so we decided to jointly fit $w_p(r_\sigma < 2$ h^{-1} Mpc) and $\hat{\xi}_{0,2}$ to search for models that could fit both adequately. The number of elements in our data vector used throughout the rest of the paper is $n_{bin} = 27$: the nine smallest scale bins in w_p as well as nine bins each for $\hat{\xi}_0$ and $\hat{\xi}_2$. The tension between the initial fits to $\xi_{0,2}$ and $\hat{\xi}_{0,2}$ naively indicates shortcomings in our model; however, as we show in Sec. 7.3, we are able to find a model within our fiducial parametrisation that adequately fits all three observables.

	fiducial	HiRes	HiRes	MedRes	COMV	COMV	high $\bar{n}_{HOD}$
$\log_{10} M_{min}$	**13.031 ± 0.029**	13.055 ± 0.022	13.089 ± 0.027	13.004 ± 0.025	13.152 ± 0.027	13.027 ± 0.027	12.926 ± 0.022
$\sigma_{\log_{10} M}$	**0.38 ± 0.06**	0.31 ± 0.05	0.38 ± 0.05	0.32 ± 0.07	0.61 ± 0.03	0.37 ± 0.06	0.16 ± 0.12
$\log_{10} M_{cut}$	**13.27 ± 0.13**	13.43 ± 0.13	13.36 ± 0.13	13.27 ± 0.14	13.07 ± 0.15	13.19 ± 0.13	13.01 ± 0.58
$\log_{10} M_1$	**14.08 ± 0.06**	14.33 ± 0.32	14.24 ± 0.18	14.09 ± 0.07	14.05 ± 0.04	14.05 ± 0.04	14.09 ± 0.05
α	**0.76 ± 0.18**	0.40 ± 0.22	0.53 ± 0.22	0.73 ± 0.20	1.03 ± 0.13	0.90 ± 0.14	0.93 ± 0.22
$\bar{n}_{HOD}$	**4.12 ± 0.13**	4.14 ± 0.11	4.08 ± 0.16	4.16 ± 0.09	4.05 ± 0.17	4.14 ± 0.11	4.64 ± 0.11
f_{sat}	**0.1016 ± 0.0069**	0.0997 ± 0.0068	0.1015 ± 0.0069	0.1015 ± 0.0071	0.1038 ± 0.0065	0.1037 ± 0.0072	0.1152 ± 0.0076
$f\sigma_8$	**0.452 ± 0.011**	**0.482**	0.449 ± 0.006	**0.472**	**0.472**	**0.472**	**0.472**
γ_{IHV}	**1.00**	**1.00**	**1.00**	**1.00**	**1.00**	**1.00**	**1.00**
γ_{cenv}	**0.00**	**0.00**	**0.00**	**0.00**	**0.00**	**0.30**	**0.00**
$\chi^2_{w_p}$ (18)	**12.4**	9.5	9.7	11.5	28.9	15.5	8.6
$\chi^2_{\hat{\xi}_{0,2}}$ (18)	**27.5**	31.0	24.4	30.6	65.0	49.4	27.1
$\chi^2_{w_p+\hat{\xi}_{0,2}}$ (27)	**32.3**	34.1	26.4	36.8	68.5	50.0	30.0
	MedRes1	MedRes2	high $\bar{n}_{HOD}$	cen/sat test	MedRes0	MedRes0	MedRes0
$\log_{10} M_{min}$	13.035 ± 0.032	13.037 ± 0.030	12.951 ± 0.030	12.983 ± 0.060	13.034 ± 0.030	13.017 ± 0.028	13.024 ± 0.030
$\sigma_{\log_{10} M}$	0.39 ± 0.06	0.39 ± 0.06	0.26 ± 0.10	0.31 ± 0.11	0.40 ± 0.07	0.34 ± 0.06	0.36 ± 0.06
$\log_{10} M_{cut}$	13.26 ± 0.14	13.28 ± 0.13	13.08 ± 0.15	11.89 ± 0.99	13.24 ± 0.13	13.24 ± 0.14	13.25 ± 0.14
$\log_{10} M_1$	14.09 ± 0.06	14.07 ± 0.06	14.06 ± 0.05	14.23 ± 0.05	14.03 ± 0.05	14.17 ± 0.10	14.08 ± 0.06
α	0.75 ± 0.19	0.75 ± 0.19	0.88 ± 0.16	1.15 ± 0.10	0.89 ± 0.15	0.67 ± 0.22	0.77 ± 0.18
$\bar{n}_{HOD}$	4.11 ± 0.14	4.11 ± 0.13	4.60 ± 0.13	3.67 ± 0.28	4.16 ± 0.09	4.10 ± 0.14	4.13 ± 0.12
f_{sat}	0.1016 ± 0.0070	0.1017 ± 0.0068	0.1140 ± 0.0074	0.1536 ± 0.0222	0.0998 ± 0.0069	0.1024 ± 0.0068	0.1021 ± 0.0070
$f\sigma_8$	0.447 ± 0.014	0.451 ± 0.010	0.458 ± 0.010	0.455 ± 0.009	0.460 ± 0.013	0.453 ± 0.011	0.445 ± 0.009
γ_{IHV}	**1.00**	**1.00**	**1.00**	**1.00**	**0.80**	**1.20**	**1.00**
γ_{cenv}	**0.00**	**0.00**	**0.00**	**0.00**	**0.00**	**0.00**	0.06 ± 0.05
$\chi^2_{w_p}$ (18)	10.9	12.5	9.9	8.3	17.4	8.4	13.4
$\chi^2_{\hat{\xi}_{0,2}}$ (18)	28.2	27.3	27.0	22.4	55.0	21.1	27.2
$\chi^2_{w_p+\hat{\xi}_{0,2}}$ (27)	31.9	32.1	28.4	22.1	57.3	24.4	32.7

Table 4. Marginalized 68% parameter constraints for under various model assumptions when fit to our measurements of $w_p(r_\sigma < 2.0\ h^{-1}$ Mpc) (9 bins) and $\hat{\xi}_{0,2}$ (18 bins). The "default" constraints are shown in bold in the first column. We also use bold to indicate parameters that were held fixed. We vary the underlying N-body simulation (HiRes, MedRes0, MedRes1, and MedRes2; where not stated, MedRes0 was used), the central galaxy velocity definition ($\mathbf{v}_{DENS}$ is the default choice, compared with $\mathbf{v}_{COMV}$ labelled "COMV"), the prior on $\bar{n}_{HOD}$ ($3.25 < 10^4 \bar{n}_{HOD}(h^{-1}$ Mpc)^3 < 4.25 is the default, "high $\bar{n}_{HOD}$" assumes $4.25 < 10^4 \bar{n}_{HOD}(h^{-1}$ Mpc)^3 < 4.75), the relation between central and satellite galaxies (the default is to assume all halos with satellites also host CMASS centrals, while Sec. 7.6 describes one alternative, labelled "cen/sat test"), and whether the velocity parameters γ_{HV} ($\propto f\sigma_8$), γ_{IHV}, and γ_{cenv} are fixed or varied. The last three rows provide the χ^2 value for the full w_p measurement (18 bins), $\hat{\xi}_{0,2}$ (18 bins), and our "default" data combination (27 bins including w_p-$\hat{\xi}_{0,2}$ covariances), evaluated at the best fit model in the MCMC chain. Experiments with a direct χ^2 minimization algorithm indicate the minimum is found within $\sim \Delta\chi^2 = 0.5$.

We planned to use only the HiRes simulation box for our theoretical calculations, but given the noisiness of the resulting likelihood surface in $f\sigma_8$, we verified our results by repeating the fits with three independent MedRes simulation boxes. Most of the final results we report are based on the MedRes0 box, but some cases using the HiRes box are presented for comparison. In general we found excellent agreement between the two.

7.2 Comparing $\mathbf{v}_{COMV}$ and $\mathbf{v}_{DENS}$ central galaxy velocity definitions

We first compare fits using two different central galaxy velocity choices, $\mathbf{v}_{DENS}$ (default) and $\mathbf{v}_{COMV}$ using the MedRes0 box. In this comparison central galaxy positions are fixed and only their velocities are varied. The prediction for $\hat{\xi}_{0,2}$ from the best fit HOD model with $\mathbf{v}_{DENS}$ (upper fourth column in Table 4) is shown in Fig. 14 in blue. To emphasize the differences caused by the choice of central galaxy velocity, we also plot the prediction for the same HOD using the center-of-mass halo velocity for central galaxies (green) and center-of-mass halo velocity plus a random Gaussian dispersion term consistent with the magnitude of $|\mathbf{v}_{DENS} - \mathbf{v}_{COMV}|$ (red); see Fig. 10. The $\mathbf{v}_{COMV}$ model is clearly a bad fit, which is also true when the HOD parameters are allowed to vary. By eye, the difference between the fiducial model and $\mathbf{v}_{COMV} + \gamma_{cenv} = 0.3$ does

not appear large compared with the square root of the diagonal elements of the covariance matrix (larger errors in Fig. 14). However, the covariance matrix has very strong correlations; to give an alternate sense of the true constraining power of our measurements, we also show a second error bar, which is the size of the change required in a single bin to change χ^2 by 1, when the model and theory differences are set to 0 in all other bins. The difference between these two "errors" is largest (a factor of 5) in the 5-17 h^{-1} Mpc bins of $\hat{\xi}_0$. Thus the data do show a strong preference for $\mathbf{v}_{DENS}$ ($\chi^2 = 36.8$) compared with either $\mathbf{v}_{COMV}$ ($\chi^2 = 68.5$; upper column five of Table 4) or $\mathbf{v}_{COMV} + \gamma_{cenv} = 0.3$ ($\chi^2 = 50.1$; upper column six), when our HOD parameters are allowed to vary and assuming the underlying halo clustering in the simulation is sufficiently similar to that in the real universe. The latter comparison indicates that the motion of the dense core of the halo relative to the center-of-mass of the halo is correlated with the surrounding cosmic structure, and this correlation propagates into the shape of the correlation function; Fig. 11 shows the alignment between the velocity difference vector and the density field around the most massive halo in the HiRes simulation. The net effect of this density-velocity correlation is to increase the redshift separation s between pairs, thus broadening both $\hat{\xi}_0$ and $\hat{\xi}_2$ compared to the uncorrelated dispersion case, $\mathbf{v}_{COMV} + \gamma_{cenv} = 0.3$. In Fig. 11, the difference vector $\mathbf{v}_{DENS} - \mathbf{v}_{COMV}$ is oriented such that it will increase the redshift
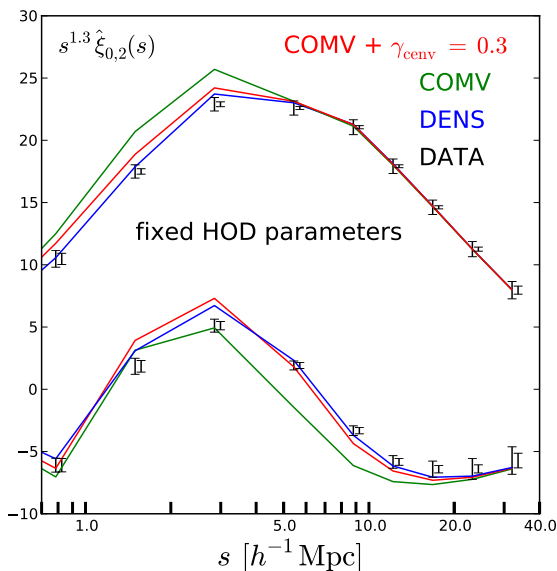
Figure 14. In order to isolate the effect of the central galaxy velocity definitions, we fix HOD parameters in this plot to the best fit values using $\mathbf{v}_{\mathrm{DENS}}$ (fourth upper column in Table 4) and plot the theoretical predictions for the fiducial choice $\mathbf{v}_{\mathrm{DENS}}$ (blue), the halo center-of-mass velocity $\mathbf{v}_{\mathrm{COMV}}$ (green), and $\mathbf{v}_{\mathrm{COMV}}$ with additional Gaussian dispersion at $0.3\sigma_{\mathrm{vir}}$ (i.e., setting $\gamma_{\mathrm{cenv}} = 0.3$; shown in red). In the other two cases, $\gamma_{\mathrm{cenv}} = 0$. In all three theoretical curves, $\gamma_{\mathrm{IHV}} = 1$ and $f\sigma_8 = 0.472$ is held fixed. We show two sets of errors: the larger ones are the square root of the diagonal elements of the covariance matrix. There are strong covariances between the bins, and the smaller error bars attempt to demonstrate their impact. The small errors show the change required in a single bin to change χ^2 by 1, when the data and theory are in perfect agreement in all other bins. Though changes between the $\mathbf{v}_{\mathrm{DENS}}$ and $\mathbf{v}_{\mathrm{COMV}} + \gamma_{\mathrm{cenv}} = 0.3$ appear relatively small, fits with the full covariance matrix disfavor the latter choice by $\Delta\chi^2 = 13$; see upper columns four through six in Table 4.

separation between the central halo and halos falling in along the corresponding filament. We saw similar levels of χ^2 differences in the HiRes box compared with the MedRes box when performing the same test. These possibilities are certainly not the only choices for assigning velocities to galaxies and neglect all "gastrophysical" effects; however, the investigations in Behroozi, Wechsler, & Wu (2013) do indicate that our $\mathbf{v}_{\mathrm{DENS}}$ has similar properties to a more detailed phase-space based halo finding algorithm.

7.3 Goodness of fit

For our fiducial choice using $\mathbf{v}_{\mathrm{DENS}}$ and the MedRes0 box for the underlying halo catalog, and introducing no free HOD velocity parameters, we find $\chi^2 = 36.8$ for 27 data points and 5 free HOD parameters; a larger χ^2 is expected only 2.5% of the time. This high χ^2 could be an indication of insufficiencies of our model, non-Gaussianity of our errors, a preference for different cosmological parameters compared with our simulation parameters, or simply bad luck. For further insight, we attempt to fit MedRes and HiRes without the theoretical error contribution to the covariance matrix. If our theoretical predictions were based on single catalog realizations rather than an average over all possible HOD realizations for a fixed halo catalog, we would expect the contribution from the measurement and MedRes theory errors to be comparable because

they cover comparable volumes. We find $\chi^2 = 75$ ($\chi^2 = 60$) to be compared with the fourth (second) columns in Table 4 for the MedRes0 (HiRes) halo catalogs. That is, our fiducial model seems adequate, within at least a factor of $\sim \sqrt{2}$ of the measurement errors. The fact that using the HiRes halo catalog, which covers only an eighth of the MedRes box volume, returns a better χ^2 in this case must indicate that changes to the observables allowed by our theoretical uncertainties can be mostly absorbed by tweaking the HOD parameters. If that were not the case, we would have expected a much larger contribution from the higher theoretical uncertainty of the HiRes box to χ^2. The slight difference could also indicate a preference of the data for the higher-resolution halo catalog. In any case, these tests do not indicate the existence of systematic modeling errors at the level of our total quoted uncertainty. Of course, just because the model can fit the data does not demonstrate that the resulting parameter fits are unbiased.

7.4 Properties of the Halo Occupation Distribution

Figure 15 shows the halo occupation distribution at the fiducial cosmologies of our HiRes and MedRes boxes (corresponding to upper columns two and four in Table 4). We enforce a hard prior on $0.1 \leqslant \alpha \leqslant 2$ which does affect the constraints from the HiRes box. Table 4 shows that the HOD parameters are quite stable as we explore different parameter spaces and model assumptions, with the exception of the "high $\bar{n}_{\mathrm{HOD}}$" and "cen/sat test" cases detailed in the next section. Within the fiducial $\bar{n}_{\mathrm{HOD}}$ prior discussed in Sec. 6.2, the data prefer the largest allowed values of $\bar{n}_{\mathrm{HOD}}$; the best fit value is near the hard prior upper boundary. Under the fiducial $\bar{n}_{\mathrm{HOD}}$ prior, the fraction of galaxies that are satellites is strongly constrained: 10.2 ± 0.7 per-cent. The data show a strong preference for a non-zero M_{cut} at a value of $\sim 2M_{\mathrm{min}}$, which could plausibly be produced by a 1:1 merger of halos of mass M_{min}. The distribution of galaxies across halo mass is relatively symmetric as a function of $\log_{10} M$ (right panel of Fig. 15), which makes the median (1.7×10^{13} h^{-1} $M_\odot$) and mean (3.3×10^{13} h^{-1} $M_\odot$) host halo masses quite different. For satellite galaxies, the median (mean) host halo mass is 6 (9) $\times 10^{13}$ h^{-1} $M_\odot$.

The mean host halo mass is most closely related to the expected amplitude of the galaxy-galaxy lensing signal. The amplitude of clustering of CMASS galaxies on scales substantially larger than a typical host halo virial radius constrains the product of a linear bias factor b and the overall amplitude of matter fluctuations $\sigma_8(z_{\mathrm{eff}})$ at the effective redshift of the galaxy sample. The observed $b\sigma_8$ for the CMASS galaxy sample places it in a halo mass regime where halo bias depends steeply on mass; $b(M)$ is overlaid in the right panel of Fig. 15. To test the robustness of the mean halo mass prediction within the context of our HOD model, we allowed a freely varying spline function to describe $dn_{\mathrm{cen}}/d\ln M$, constrained by a minimum $\bar{n}_{\mathrm{HOD}}$ set by the observed $\bar{n}(z)$ and constrained to reproduce the observed $b\sigma_8$. Adding this freedom to the HOD only introduced uncertainty in the mean central galaxy halo mass at the $\sim 10\%$ level.

The high-mass slope α of the satellite HOD is not well-constrained in our fits, and in particular, our $\alpha >= 0.1$ prior affects the constraints in the HiRes case. However, the satellite galaxy distributions in the right panel of Fig. 15 are similar, and the corresponding intra-halo velocity dispersion is well-constrained by our measurements; see Sec. 7.9.
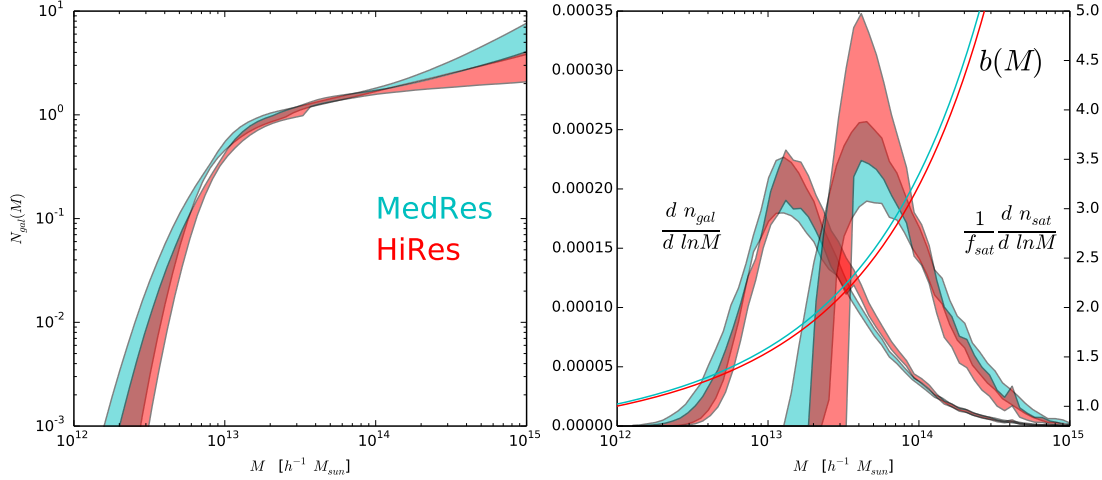
Figure 15. Assuming the cosmology for the MedRes (cyan) or HiRes (red) simulation boxes, we show the halo occupation distribution of CMASS galaxies as a function of host halo mass. These HODs have $\bar{n}_{HOD} = 4.15 \pm 0.1$ $[h^{-1}$ Mpc$]^{-3}$, while the typical $\bar{n}$ for the CMASS redshift distribution is somewhat lower (see Fig. 12). Our model assumes that the observed CMASS sample is a random subsample of this HOD. Multiplying by the halo mass function in the two simulations gives the probability distribution of galaxies as a function of host halo mass (left curves in right panel). We also show the distribution of satellite galaxies separately, rescaling by f_{sat} for visualization purposes. Finally, we overlay the Tinker et al. (2010) $b(M)$ relation for the two cosmologies. At fixed mass, halos in the HiRes simulation are slightly less biased since σ_8 and Ω_m are slightly larger in that simulation.

Neglecting slight differences in cosmological parameters, we find excellent agreement with the analysis of $w_p(0.3h^{-1}$ Mpc $< r_\sigma < 30h^{-1}$ Mpc) in White et al. (2011). Converting to our HOD parameter definitions, their Table 2 implies $\sigma_{log_{10}M} = 0.30 \pm 0.07$, $log_{10}M_{\min} = 13.08 \pm 0.12$, $\log_{10} M_1 = 14.06 \pm 0.1$, $M_{cut}/M_{\min} = (1.13 \pm 0.38)$, $\alpha = 0.9 \pm 0.19$, and $f_{sat} = 10 \pm 2$ per-cent. We find $M_{cut}/M_{\min} = (1.8 \pm 0.6)$. Since White et al. (2011) used one-tenth the sky area of the DR10 analysed in this paper and we have added information from $\hat{\xi}_{0,2}$, it is rather surprising that our errors on most parameters seem comparable. Some of the difference can likely be attributed to our conservative estimate on the angular upweighting errors that dominate the error budget in the one-halo region of w_p, our wider prior on $\bar{n}_{HOD}$, and our inclusion of a theoretical error budget. Our measurements do improve the errors considerably on the satellite fraction and the $N_{cen}(M)$ mass scale. The latter is expected since the larger survey volume and inclusion of ξ_0 allow a precise clustering amplitude measurement on large scales. We also note that Nuza et al. (2013) showed relatively good agreement between the observed DR9 CMASS clustering and the predictions of SHAM; their resulting CMASS HOD is also in broad agreement with the results of White et al. (2011) as well as those presented here. We note that our estimate of ξ_0 derived in Sec. 4 and the Nuza et al. (2013) measurement, based on the Guo, Zehavi, & Zheng (2012) fiber collision correction method, significantly disagree on scales between 1 and 8 h^{-1} Mpc. Finally, we note that Guo et al. (2014) have recently used the Guo, Zehavi, & Zheng (2012) fiber-collision correction method to compute the projected clustering w_p of various luminosity, redshift, and color subsamples of CMASS. Our results are not directly comparable because of their cuts, but a cursory examination yields some interesting differences. Their M_0 parameter (equivalent to our M_{cut}) is constrained to be effectively 0, while our constraints require it to be at least larger than $M_{\min}$. Their CMASS subsample with $M_i > -21.6$ and $0.48 < z < 0.55$ has the largest $\bar{n}$ among their subsamples (still a factor of two lower than our best fit HODs), and yet has more satellites per halo than
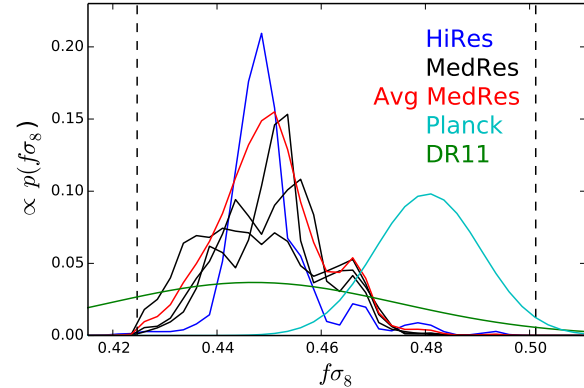

Figure 16. The marginalized distribution of $f\sigma_8$ from our HiRes box (blue) and three MedRes boxes (black; red shows their average). In this case $\gamma_{cenv} = 0$ and $\gamma_{IHV} = 1$ were held fixed. We compare this to the constraints from Planck ΛCDM fits ($f\sigma_8 = 0.480 \pm 0.010$) and our DR11 analysis of the CMASS galaxy clustering restricted to large scales $s > 25$ h^{-1} Mpc, where we found $f\sigma_8 = 0.447 \pm 0.028$. Vertical dashed lines show our hard prior on the MedRes box of $\pm 10\%$ of the $f\sigma_8$ value in the MedRes cosmology.

our HOD for masses above $\sim 10^{14.6}$, despite their lower $f_{sat} = 7.9$ per-cent. An examination of the anistropic clustering in their samples may shed light on this difference. Their analytic HOD model is calibrated on FoF halo catalogs, and may therefore require more satellites in massive halos than our model, since SO halo catalogs have more halo pairs near the one-halo to two-halo transition.

7.5   Fits to $f\sigma_8(z = 0.57)$

Next, we consider the effect of linearly varying the overall amplitude of the peculiar velocity field with the parameter γ_{HV}, and interpret the result as a change in the effective $f\sigma_8$. We justify this
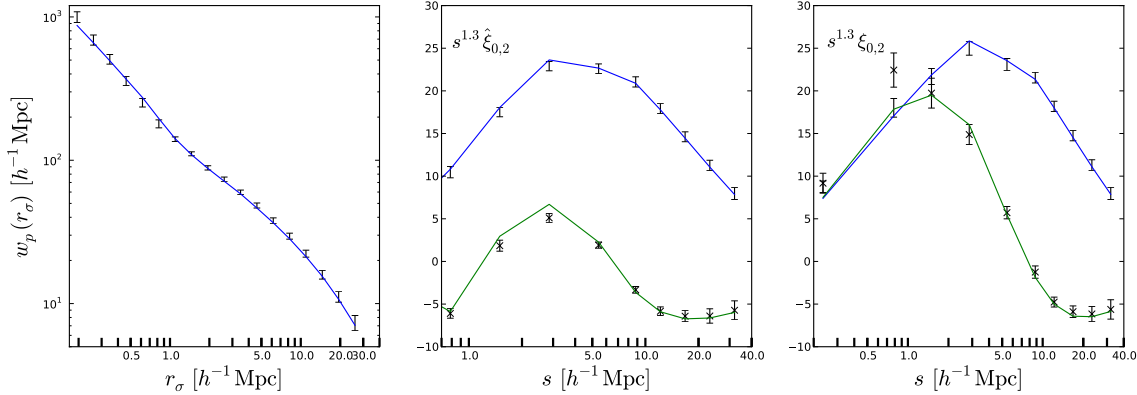
Figure 17. The best fit model using the "MedRes0" box, fixing $\gamma_{\mathrm{IHV}} = 1$ and $\gamma_{\mathrm{cenv}} = 0$ compared to our measurements for w_p, $\hat{\xi}_{0,2}$, and $\xi_{0,2}$ (bottom first column of Table 4). In the second two panels $\hat{\xi}_2$ and ξ_2 measurements are indicated with an X, and the model predictions with green curves instead of blue, since ξ_0 and ξ_2 cross on small scales. The varying parameters took best fit values $f\sigma_8 = 0.452$, $M_{\mathrm{min}} = 10^{13.011}$ h^{-1} $M_\odot$, $M_{\mathrm{cut}} = 10^{13.159}$ h^{-1} $M_\odot$, $M_1 = 10^{14.068}$ h^{-1} $M_\odot$, $\alpha = 0.89$, $\sigma_{\log_{10} M} = 0.358$. This HOD has $\bar{n}_{\mathrm{HOD}} = 4.23 \times 10^{-4}$ $(h^{-1}\,\mathrm{Mpc})^{-3}$ and $f_{sat} = 10.4$ per-cent. The best fit χ^2 values are listed in the first lower column in Table 4. This best fit model is derived by fitting only the first nine bins of w_p and $\hat{\xi}_{0,2}$, but also provides a good fit to $\xi_{0,2}$, for which $\chi^2 = 20.9$ for 20 measurement bins. Compared to the best fit with $\gamma_{\mathrm{HV}} = 1$ ($f\sigma_8 = 0.472$), the fit to the quadrupole on large scales is improved. Our last 1.5 bins overlap with the smallest bins in the large-scale RSD analysis in Reid et al. (2012) and Samushia et al. (2013) and our best fit $f\sigma_8$ values are nearly identical.

interpretation in Sec. 7.7. Here we consider only the case when the other velocity parameters $\gamma_{\mathrm{cenv}} = 0$ and $\gamma_{\mathrm{IHV}} = 1$ are held fixed. The marginalized distribution of $f\sigma_8$ shown in Fig. 16 is clearly noisy due to the finite volume of our N-body simulation boxes. We therefore computed constraints separately from three independent MedRes boxes (labelled Fiducial=MedRes0, MedRes1, and MedRes2 in Table 4) as well as with the single HiRes box we had available (top row, third column in the table). The marginalized $f\sigma_8$ constraints are consistent across the boxes, despite the $\sim 1\sigma$ shift in fiducial value between the box cosmologies. Averaging over the MedRes simulation boxes, we find $f\sigma_8 = 0.450 \pm 0.011$, consistent with our recent large-scale analysis of DR11 (Samushia et al. 2013) which found $f\sigma_8 = 0.447 \pm 0.028$ for a ΛCDM expansion history. Our raw statistical error is equal to Planck's ΛCDM prediction of $f\sigma_8 = 0.48 \pm 0.010$; the difference between the two independent measurements is 1.9σ, which we take to be reasonable agreement since we have not included a modeling systematics error budget. Despite the dominance of satellite galaxies on the observed anisotropies (Fig. 13), there is still ample information on the rate of structure growth on these smaller scales where the clustering signal is strong and well-measured, resulting in a factor of 2.5 reduction in uncertainty on $f\sigma_8$ compared with our DR11 large-scale RSD analysis. In Fig. 17 we show the theoretical prediction from the best fit model using the MedRes0 box. In this model $f\sigma_8 = 0.452$ and we have held $\gamma_{\mathrm{IHV}} = 1$ and $\gamma_{\mathrm{cenv}} = 0$ fixed. Compared to the best fit model with $\gamma_{\mathrm{HV}} = 1$ ($f\sigma_8 = 0.472$) in Fig. 14, the amplitude of ξ_2 on large scales provides a better fit to the data. These are the same scales dominating the Samushia et al. (2013) large-scale RSD measurement of $f\sigma_8$; the last ~ 1.5 bins overlap between the analyses. The best fit models as a function of $f\sigma_8$ have nearly identical behavior in the first three bins $s < 3$ h^{-1} Mpc, and divide on larger scales, indicating that the constraint on $f\sigma_8$ is driven by the relative amplitudes of $\hat{\xi}_0$ and $\hat{\xi}_2$. Fig. 17 also shows that even though the model was fit to $w_p(r_\sigma < 2$ h^{-1} Mpc) and $\hat{\xi}_{0,2}$, it provides a good fit to w_p out to 25 h^{-1} Mpc ($\chi^2 = 12.4$ for 18 bins), and correctly models scales below the fiber collision radius, so that $\xi_{0,2}$ is also fit ($\chi^2 = 20.9$ for 20 bins).

7.6 Robustness of the $f\sigma_8$ constraint to model extensions

The basic redshift-independent HOD model we are using to fit the CMASS clustering assumes that the observed galaxies are a subsample of objects defined by those HOD parameters. We enforce only a broad prior on $\bar{n}_{\mathrm{HOD}}$ from the observed CMASS selection function $\bar{n}(z)$. However, both intrinsic stochasticity in the stellar mass-halo mass relation and photometric errors in the imaging catalog will broaden the distribution of halo masses hosting the CMASS sample. In order to test our sensitivity to the allowed host halo mass scatter, we refit our measurements with the $\bar{n}_{\mathrm{HOD}}$ prior shifted to higher values: $4.25 < 10^4 \bar{n}_{\mathrm{HOD}}(h^{-1}\,\mathrm{Mpc})^3 < 4.75$. The results of fits that fix or vary $f\sigma_8$ are labelled in Table 4 as "high $\bar{n}_{\mathrm{HOD}}$." This choice is similar to relaxing our assumption that $N_{\mathrm{cen}}(M)$ in Eq. 17 approaches one at large halo masses. Indeed, we find that this region of HOD parameter space provides a better fit to the observed clustering ($\Delta\chi^2 \sim 4$). There are small (expected) shifts in the HOD parameters with the higher $\bar{n}_{\mathrm{HOD}}$ prior; most importantly for our conclusions in this work, the constraint on $f\sigma_8$ shifts by only $\sim 0.5\sigma$. If we completely remove the $\bar{n}$ prior, the HOD is limited to $10^4 \bar{n}_{\mathrm{HOD}}(h^{-1}\,\mathrm{Mpc})^3 < 6$ as $\sigma_{\log_{10} M}$ approaches 0, which is an unphysical limit of noisy target selection producing a precise mass cut in central galaxy host mass. Given our HOD parametrization, models with higher number density are unable to generate sufficiently large clustering. Even in this unrealistic case, the $f\sigma_8$ shifts upward compared to our fiducial value by only 1σ.

Both the color selection and photometric errors in the imaging used for target selection could result in halos where the central galaxy does not pass our target selection cuts, while one or more satellite galaxies in that halo do pass. To test the impact of such cases (labelled "cen/sat" test in Table 4), we consider the drastic case where 20% of centrals in massive halos are not CMASS selected galaxies, implemented in our model by simply multiplying $N_{\mathrm{cen}}(M)$ by 0.8. In contrast to the rest of our analyses, in this test we do not require a central galaxy in order for a particular halo to host a satellite galaxy, thus lowering the contribution of "one-halo" central-satellite pairs at fixed HOD parameters. This model provides a much better fit than our fiducial HOD assump-

tions ($\Delta\chi^2 = 10.2$). The satellite fraction is larger, $\bar{n}_{\text{HOD}}$ in the model moves closer to the typical $\bar{n}$ in the sample, and the satellite occupation distribution steepens. In future work we hope to explore such model extensions more generally in concert with a better understanding of the impact of photometric errors on targeting, as well as redshift evolution and intrinsic diversity in the CMASS galaxy population. Again, the important result for the present work is that a plausible extension of our halo occupation modeling can improve the fit, but the constraint on $f\sigma_8$ shifts only slightly.

Next we consider the impact of varying the galaxy intrahalo velocities through the parameters γ_{IHV} and γ_{cenv} defined in Sec. 6.3. Their impact on the $\hat{\xi}_{0,2}$ observable is shown in Fig. 18, holding the HOD parameters fixed to the best fit values for $\gamma_{\text{HV}} = \gamma_{\text{IHV}} = 1.0$ and $\gamma_{\text{cenv}} = 0$. Increasing the intrahalo velocity dispersion lowers the number of pairs at small s separations, while changing $f\sigma_8$ shifts the peak position in $s^{1.3}\hat{\xi}_0$. The impact of γ_{IHV} on $\hat{\xi}_2$ extends out to much larger scales than γ_{cenv}, as expected because intrahalo satellite velocities have a broader dispersion than centrals. Changing $f\sigma_8$ has a distinct scale dependence in both $\hat{\xi}_0$ and $\hat{\xi}_2$, which should be distinguishable from γ_{IHV} and γ_{cenv}.

We introduce the parameter γ_{IHV} to rescale the relative velocity between satellite galaxies and their host halos. This parameter is meant to absorb the effect of galaxy velocity bias as well as variations in the halo mass function due to cosmological parameter uncertainties. White Cohn, & Smit (2010) examine in detail the velocity structure of subhalos within group-scale halos at z=0.1, and suggest a theoretical uncertainty in velocity bias of $O(10\%)$. Wu et al. (2013) used N-body and hydrodynamical simulations to study the relationship between the galaxy and dark matter intrahalo velocity dispersion in halos of mass $\sim 10^{14}\, M_\odot$, i.e., well-matched to the typical satellite galaxy host halo mass according to our HOD model fits. They found that averaging over all cluster galaxies, $\sigma_{\text{IHV,gal}}/\sigma_{\text{IHV,DM}} = 1.065$, while averaging only over the five brightest satellites yielded a ratio of 0.868. The latter is likely more applicable to the massive galaxies comprising the CMASS sample. Rather than smoothly varying γ_{IHV}, we run separate MCMC chains at $\gamma_{\text{IHV}} = 0.8$ and $\gamma_{\text{IHV}} = 1.2$; this range incorporates the small velocity biases found in Wu et al. (2013). Alternatively, neglecting velocity bias, a ± 20 per-cent variation in γ_{IHV} corresponds to a factor of 0.5-1.7 change in the host halo mass scale of satellite galaxies. The fifth and sixth bottom columns of Table 4 show the result of these fits; $\gamma_{\text{IHV}} = 0.8$ is strongly disfavored by our data ($\Delta\chi^2 = 25$), but the best fit of $f\sigma_8$ under this assumption is still in good agreement with our fiducial case at the 1σ level. Our data shows a $\Delta\chi^2 = 8$ preference for $\gamma_{\text{IHV}} = 1.2$, indicating that our fiducial model may not produce strong enough finger-of-god features. Again, allowing freedom in γ_{IHV} does not shift or weaken the constraining on $f\sigma_8$.

Finally, we also introduce additional random velocity dispersion for central galaxies through the parameter γ_{cenv} (final bottom column of Table 4). The fiducial value $\gamma_{\text{cenv}} = 0$ is preferred by the data. Allowing γ_{cenv} as a free parameter shifts the 68% confidence region on $f\sigma_8$ lower by $\sim 0.5\sigma$. We do note that preliminary tests using the HiRes box showed that when both γ_{IHV} and γ_{cenv} are free (and both take large values outside the range considered here), the best fit value of $f\sigma_8$ is more dramatically reduced. The statistical precision of our fiducial $f\sigma_8$ constraint certainly warrants a further assessment of our uncertainties of the velocity structure of CMASS-type galaxies relative to their host dark matter halos. Appendix B showed that the velocity of the halo center is not well-defined, but depends on the averaging scale. We have chosen a scale that roughly matches the size of the typical CMASS galaxy, but
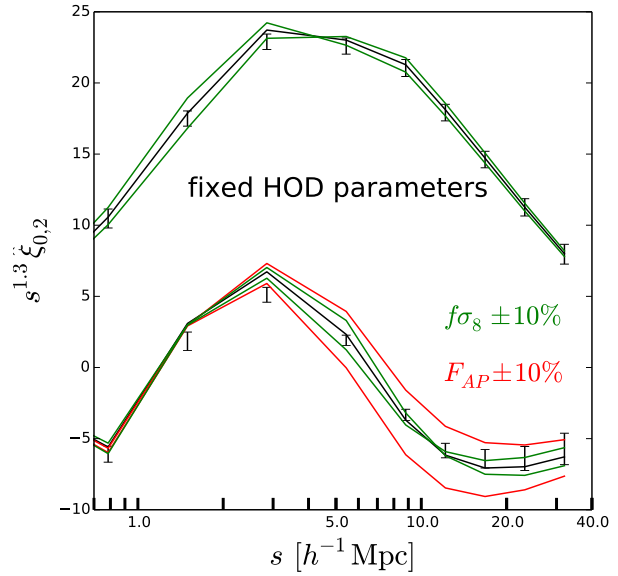

Figure 19. Predictions for $\hat{\xi}_{0,2}$ when the growth rate of structure $f\sigma_8$ or the geometric Alcock-Paczynski parameter F_{AP} is varied by 10%, at fixed HOD parameters. In the latter case, we also held fixed the isotropic BAO scale $\propto D_A^{2/3} H^{-1/3}$, so that the prediction for $\hat{\xi}_0$ is unchanged and thus not shown. F_{AP} is tightly constrained assuming a flat ΛCDM expansion history, but more general dark energy models will modify both $f\sigma_8$ and F_{AP}. Our current results therefore cannot yet be applied to constraining dark energy.

ideally the uncertainty associated with this choice (and the potential impact of baryonic effects) should be accounted for in future work.

7.7 Non-linear velocities, cosmology dependence and light-cone effects

With the single exception of the cosmological parameter combination determining $f\sigma_8$, we have not explored how our constraints depend on cosmological parameters. In this section we merely discuss where the largest sensitivities lie. Under the assumption of adiabatic fluctuations and the standard three species of massless neutrinos, the CMB observations tightly constrain the power spectrum of matter fluctuations (Planck Collaboration 2013) with k in units of Mpc; under these assumptions, $P(k)$ depends only on physical densities $\Omega_{c,b,\gamma}h^2$ and n_s (see Section 5.1.1 of Reid et al. 2012). These tight constraints on the linear matter power spectrum should translate to strong constraints on the scale-dependence of halo clustering as well. As in other analyses simultaneously fitting cosmology and HOD-like parameters (Tinker et al. 2011; Cacciato et al. 2013; Mandelbaum et al. 2013), we naively expect most of our sensitivity to cosmological parameters to be through some combination of σ_8 and Ω_m.

We have allowed the overall amplitude of the halo peculiar velocity field in our simulations to vary, and in Sec. 7.5 have interpreted this amplitude as a constraint on $f\sigma_8$. This linear scaling is expected to break down in the non-linear regime; recall, for instance, that perturbative corrections to the power spectrum are proportional to powers of the linear growth factor (D^2, D^4, ...) times different functions of k. To check the impact of both light cone effects and the $f\sigma_8$ scaling approximation, we examine halo cat-

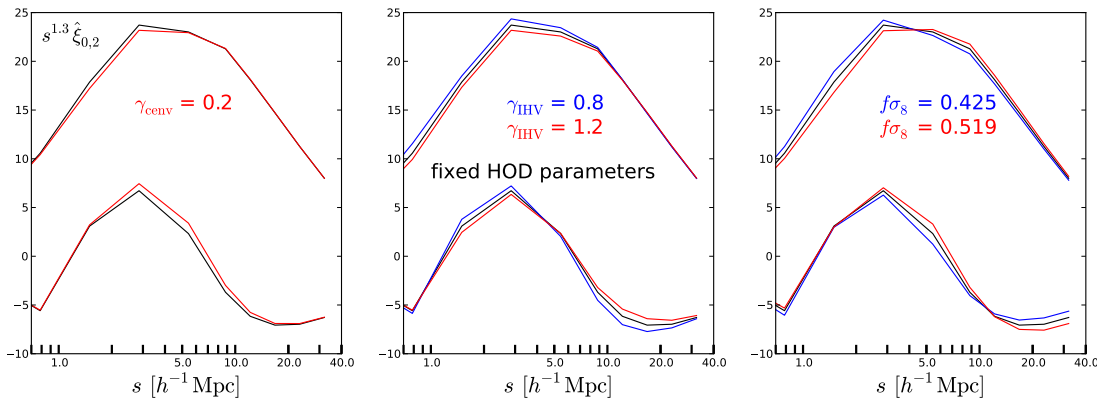**Figure 18.** The impact on $\hat{\xi}_{0,2}$ of varying the three velocity rescaling parameters γ_{cenv}, γ_{IHV}, and $\gamma_{\mathrm{HV}} \propto f\sigma_8$ at fixed HOD parameters.

alogs from the MedRes0 box at neighboring redshift outputs: $z = 0.45, 0.55, 0.65$, for which $\sigma_8(z) = 0.59, 0.62, 0.65$. Thus the edges span a 10% change in the large-scale amplitude of matter fluctuations. We divide our fiducial halo catalog at $z = 0.55$ into four mass bins split on the cumulative mass distribution from our best fit HOD model with boundaries edges at [10%, 30%, 50%, 70%, 90%]. Motivated by our observation in Appendix A that there is no measurable redshift evolution of the CMASS clustering, we shift these mass bins slightly at $z = 0.45$ and $z = 0.65$, with the bin centers shifted to match the large scale value of $b(M)\sigma_8(z)$ in the original bins. The difference in the corresponding mass bin centers between the $z = 0.45$ and $z = 0.65$ outputs was at most 20%, for a 10% change in σ_8 across this redshift range. Across this same redshift range, we measure the normalization of the $\sigma_{\mathrm{vir}}(M)$ relation to decrease by 7%. These two effects nearly cancel each other, so for HODs selecting halos with the same distribution of $b\sigma_8$, the effective γ_{IHV} will remain ≈ 1 at the-percent level, well within the range $\pm 20\%$ explored in the previous section. We expect small changes in other cosmological parameters to be within this prior as well. With these mass bins we can also compare the clustering and velocity statistics at different redshifts. By design, our bins have the large-scale clustering amplitude matched, so we can isolate the impact of non-linear growth on the underlying halo clustering. We first compare the matched real space correlation functions and pairwise infall velocities across redshift. Changes in non-linear growth to $\xi(r)$ and $v_{12}(r)$ at fixed large scale $b\sigma_8$ is not well-detected in this measurement using a single simulation box, but is constrained to be smaller than $\pm 2\%$, except in the largest halo mass bin ($10^{13.43} - 10^{13.82}\ h^{-1}M_\odot$), where the real and redshift-space monopoles change by ~ 10 and ~ 15 per-cent respectively below 1 h^{-1} Mpc in the expected directions. We detect no significant trends in $\hat{\xi}_2$. We conclude that at fixed cosmological parameters (other than σ_8), non-linear corrections to the theoretical template can be neglected when inferring $f\sigma_8$. Since the relevant halo clustering is so similar at the three redshifts, we infer that light-cone effects should have a negligible impact on our theoretical template. That is, our theoretical template from a fixed redshift output should be nearly the same as if we had generated it from a light cone (after perhaps small shifts in HOD parameters).

We have tested this assertion by refitting the measurements using the halo catalog from the MedRes box output at $z = 0.65$, where σ_8 is 5% lower than at our fiducial $z = 0.55$. The matter clustering in this redshift slice should be closer to the clustering in

a model with the overall amplitude of fluctuations lowered to match our best fit $f\sigma_8$. However, the value of $f\sigma_8$ in the higher redshift slice is only smaller by 1% since $\Omega_m(z)$ increases with redshift. Accounting for this difference, we find $f\sigma_8 = 0.449 \pm 0.008$, in excellent agreement with our fiducial fit using the $z = 0.55$ halo catalog.

One additional impact of cosmological parameters is in the conversion of angles and redshifts into comoving coordinates. As in Anderson et al. (2013) and Samushia et al. (2013), we assume a cosmology with $\Omega_m = 0.274$ and $h = 0.7$ for this conversion. We did not account for the difference between the fiducial cosmology and simulation cosmology in the theoretical model, but the error on the angle-averaged distance scale $D_V \propto D_A^{2/3}(z_{\mathrm{eff}})H^{-1/3}(z_{\mathrm{eff}})$ in h^{-1} Mpc units is only 1.0%. We checked that this error has a negligible impact on our theoretical predictions: the difference amounts to $\Delta\chi^2 = 0.9$ at fixed HOD parameters. The Alcock-Paczynski (Alcock & Paczynski 1979) parameter $F_{AP} \propto D_A(z_{eff})H(z_{eff})$ distorts line-of-sight distances relative to transverse distances and at fixed D_V, a change in F_{AP} alters ξ_2 while holding ξ_0 basically fixed. Fig. 19 compares the impact of 10% changes in $f\sigma_8$ and F_{AP} on $\hat{\xi}_2$ at fixed HOD parameters; changes caused by the two parameters are distinguishable because of their differing scale dependence. Allowing uncertainty in F_{AP} will however degrade our constraints on $f\sigma_8$; in Reid et al. (2012) and Samushia et al. (2013) we report joint constraints on $f\sigma_8$-F_{AP}. Since geometric parameters are "slow" variables in our theoretical calculation (they alter the separation between halo pairs), we defer a joint $F_{AP} - f\sigma_8$ constraint to future work. Note that non-cosmological constant dark energy affects both geometric and growth of structure parameters, so our measurement of $f\sigma_8$ cannot be used to constrain dark energy without accounting for this degeneracy. The current work can be considered only a consistency test of the ΛCDM + general relativity model, where F_{AP} is constrained to within 0.6% (Planck Collaboration 2013). At fixed cosmological and HOD parameters in our model, varying F_{AP} by 1.2% produces a change in the theoretical prediction of $\Delta\chi^2 = 1$, so we can safely neglect this uncertainty when testing models that assume a flat ΛCDM expansion history.

7.8 Sensitivity of $f\sigma_8$ constraint to small scales

Finally, we assess the sensitivity of our $f\sigma_8$ constraint to the small-scale velocity distribution probed by $\hat{\xi}_{0,2}$ by performing fits to $w_p(r_\sigma < 2\ h^{-1}\ \mathrm{Mpc}) + \hat{\xi}_{0,2}(s < 10.3\ h^{-1}\ \mathrm{Mpc})$ and $w_p(r_\sigma < 2$
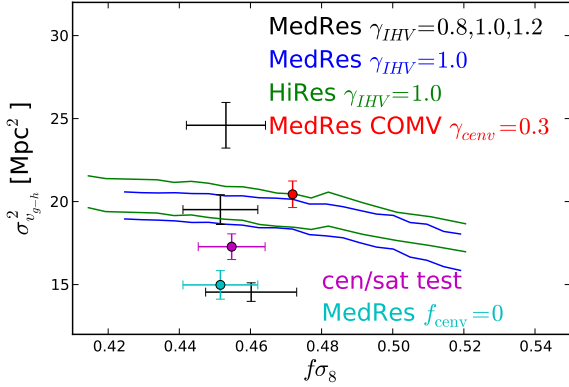
Figure 20. Second moment of the velocity dispersion of centrals and satellites relative to the center-of-mass velocity of their host dark matter halos computed from the HOD constraints presented in Table 4. Ignoring the goodness-of-fit, we find the dependence of $\sigma_{v_{g-h}}$ as a function of $f\sigma_8$ using several chains at fixed $f\sigma_8$ values. The MedRes (blue) and Hires (green) fits give similar results. The black points show the constraints from the chains that vary $f\sigma_8$ at fixed $\gamma_{\mathrm{IHV}} = 0.8, 1.0, 1.2$ using the MedRes0 simulation box. Larger γ_{IHV} corresponds to a larger $\sigma_{v_{g-h}}^2$. Neglecting the fiducial central galaxy dispersion moves the central black constraint to the cyan one, demonstrating that central galaxy intra-halo velocities are non-negligible. Finally, we obtain a similar value for $\sigma_{v_{g-h}}^2$ when we assign central galaxies the center-of-mass velocity of their halo and then add velocity dispersion with $\gamma_{\mathrm{cenv}} = 0.3$ (red) or when using the model described in Sec. 7.6 as the "cen/sat" test (magenta). $\sigma_{v_{g-h}}$ should be directly related to the nuisance parameter σ_{FOG}^2 used in Reid et al. (2012) and Samushia et al. (2013).

h^{-1} Mpc) $+ \hat{\xi}_{0,2}(s > 10.3 \ h^{-1}$ Mpc); that is, the first (second) choice combines our fiducial w_p measurements with the first five (last four) s bins of our $\hat{\xi}_{0,2}$ measurement. The first fit essentially recovers the results of our fiducial fit including all s bins to nearly the same precision, implying that essentially all of our $f\sigma_8$ information comes from these non-linear scales and therefore potentially sensitively depends on the accuracy of our HOD modeling approach. Table 4 shows that for a reasonable range of extensions to our fiducial model, the $f\sigma_8$ constraint is stable.

The fit restricted to larger s bins has considerable shifts in HOD parameters. While the satellite fraction is still well-constrained with the same central value, the distribution of the satellites shifts to lower halo masses. Rather than a constraint on M_{cut}, this fit prefers $log_{10}M_{\mathrm{cut}} < 13.04$ with 95% confidence, $log_{10}M_1$ increases by 0.2, and $\alpha = 1.07\pm0.12$. This HOD model has weaker FOG features, which therefore lowers $f\sigma_8$ to 0.435 ± 0.033 but also alters $\hat{\xi}_{0,2}$ on small scales. The best fit to $w_p(r_\sigma < 2 \ h^{-1}$ Mpc) $+ \hat{\xi}_{0,2}(s > 10.3 \ h^{-1}$ Mpc) is strongly disfavored using our fiducial set of measurements ($\chi^2 = 70$).

7.9 Predicting σ_{FOG}^2

In Reid et al. (2012) and Samushia et al. (2013), we analysed the large scale $\xi_{0,2}$ with an analytic Gaussian streaming model to constrain $f\sigma_8$ along with geometric parameters $D_A(z_{\mathrm{eff}})$ and $H(z_{\mathrm{eff}})$. The model has a single parameter, σ_{FOG}^2, to account for the effect of small-scale motions, like satellite galaxies within their host halos (traditional "fingers-of-god"). The model convolves the predicted halo auto-correlation function with a Gaussian, approximating the velocities of galaxies relative to their host halos as uncorrelated with the quasilinear flows of interest. We can estimate the proba-
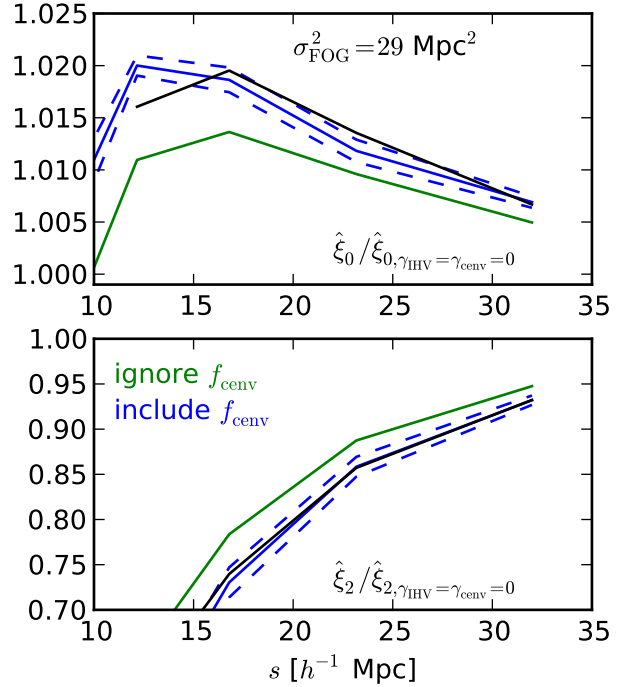

Figure 21. We use the ratios $\hat{\xi}_\ell/\hat{\xi}_{\ell,\gamma_{\mathrm{IHV}}=\gamma_{\mathrm{cenv}}=0}$ for $\ell = 0, 2$ as a proxy for the nuisance parameter σ_{FOG}^2. These ratios are tightly constrained by our measurements (blue bands). For this purpose we compute the theoretical prediction using the center-of-mass velocity $\mathbf{v}_{\mathrm{COMV}}$ for the central galaxies to account for the dispersion in $\mathbf{v}_{DENS} - \mathbf{v}_{\mathrm{COMV}}$; neglecting this term produces the green curves. We compute the analogous quantity using *cosmoxi2d* as a function of nuisance parameter σ_{FOG}^2, recovering 29 Mpc^2 as the best fit for the case where $\gamma_{\mathrm{IHV}} = 1.0$ and $f\sigma_8$ is allowed to vary. Reassuringly, the *cosmoxi2d* model reproduces the scale-dependence of this ratio as measured from our HOD model predictions.

bility distribution function of those velocities, assuming the central galaxies also have some residual motion specified by a fraction f_{cenv} of the halo virial velocity. Using the halo model and assuming a central is required for a halo to host a satellite, we can estimate the probability distribution of galaxy velocities relative to their host halos as

$$p(\Delta v_{g-h}) = n_{tot}^{-1} \int dM n(M) N_{\mathrm{cen}}(M) \times$$

$$\left[G\left(\Delta v_{g-h}, f_{\mathrm{cenv}}\sigma_{\mathrm{vir}}^2(M)\right) + N_{sat}(M)G\left(\Delta v_{g-h}, \sigma_{\mathrm{vir}}^2(M)\right)\right], \quad (20)$$

where $G(\Delta v_{g-h}, \sigma^2)$ is a Gaussian probability distribution with variance σ^2 and mean 0, and $n(M)$ is the halo mass function. To get the pairwise velocity distribution component due to galaxy motions relative to the center-of-mass velocity of their host halos for pairs in different host halos, we convolve Eq. 20 with itself. The result has a narrow distribution about $\Delta v_{g-h} = 0$ from central galaxy pairs, and an exponential tail due to the much larger satellite galaxy velocities. We can evaluate the second moment of this distribution, $\sigma_{v_{g-h}}^2$, at each point in our chains to determine its mean and uncertainty. 68% confidence intervals are shown in Fig. 20 as a function of $f\sigma_8$ for both the HiRes (green) and MedRes (blue) simulations over a broader range of $f\sigma_8$ values than is preferred by our fiducial MedRes fits (central black point, with 68% confidence in $f\sigma_8$ also shown). The plot shows that $\sigma_{v_{g-h}}^2$ is very well constrained by our

measurements and has only a modest degeneracy with $f\sigma_8$. Varying the satellite galaxy relative velocities by γ_{IHV} by $\pm 20\%$ (upper and lower black points) also changes $\sigma^2_{v_{g-h}}$ by 25%; note from Table 4 that $\gamma_{IHV} = 0.8$ provides a poor fit to our measurements of $\hat{\xi}_{0,2}$. Also shown in red is the constraint derived from a MedRes chain adopting center-of-mass velocities for central galaxies, but adding a random dispersion to central galaxies of magnitude $0.3\sigma_{vir}$ and holding $\gamma_{HV} = 1$ fixed. The "cen/sat test" model (magenta point) described in Sec. 7.6 relaxes the assumption that halos hosting satellite CMASS galaxies also always host centrals; this model produces a similar value of $\sigma^2_{v_{g-h}}$ as our fiducial one. Finally, we can also separate the contributions from central and satellites to the dispersion in Eq. 20. In our default chain, we find the central term to contribute 4.5 ± 0.1 and the satellite term to contribute 15.0 ± 0.9 (shown in cyan on the figure). It is therefore imperative to allow for some dispersion in both the central and satellite galaxies, relative to the bulk halo motion. To incorporate a reasonable uncertainty on γ_{IHV} and γ_{cenv}, we suggest a conservative Gaussian prior on $\sigma^2_{v_{g-h}}$ centered at 19.5 Mpc^2 and with uncertainty of $\sqrt{2} \times 5$ Mpc^2 to account both for 1σ uncertainty corresponding to γ_{IHV} uncertain by 20% and central galaxy dispersion uncertain at the 100% level.

Before we can apply this prior to our analysis of large scale clustering, we need to understand the relation between the nuisance parameter σ^2_{FOG} and $\sigma^2_{v_{g-h}}$, which we estimate from the HOD constraints from small scale clustering; the relation is non-trivial due to the non-Gaussianity of $p(\Delta v_{g-h})$. Unfortunately, constraints on σ^2_{FOG} by fitting mock catalogs directly with *cosmoxi2d* (the theoretical prediction software used in Reid et al. 2012 and Samushia et al. 2013) on the same large scales as the data is extremely noisy, even at known $f\sigma_8$ and geometric parameters. We remove much of the cosmic variance in the inference of σ^2_{FOG} from mock catalogs by considering the ratios $\hat{\xi}_{0,2}/\hat{\xi}_{0,2,\gamma_{IHV}=\gamma_{cenv}=0}$. In particular, we assign center-of-mass halo velocities to the central galaxies to compute the denominator but use $\mathbf{v}_{DENS}$ in the numerator, since we found the first term in Eq. 20 is not negligible, and the majority of perturbation theory models (including *cosmoxi2d*) are validated using halo catalogs containing $\mathbf{v}_{COMV}$. The resulting ratio is shown in blue in Fig. 21 for the MedRes box. A 68% error band shown as blue dashed curves are derived from the uncertainty on the HOD parameters using the default chain with $\gamma_{IHV} = 1.0$, $\gamma_{cenv} = 0$, and γ_{HV} free; comparison with two additional MedRes boxes indicates that cosmic variance is a subdominant contribution to the uncertainty for the ratio.

We compute an analogous ratio using *cosmoxi2d*, varying σ^2_{FOG} in the numerator and setting it to 1 Mpc^2 in the denominator, consistent with the expected value for halos reported in Reid & White (2011). *cosmoxi2d* is based on perturbation theory, and the underlying model for halo clustering breaks down at ~ 25 h^{-1} Mpc. We therefore determine the best fit σ^2_{FOG} using only the last bin in our small-scale measurements, 27-38 h^{-1} Mpc and find $\sigma^2_{FOG} = 29 \pm 2$ Mpc^2. Fig. 21 shows that the scale-dependent distortions to $\xi_{0,2}$ caused by the relative velocities between halos and galaxies is described well by the nuisance parameter σ^2_{FOG}, even to smaller scales than included in the *cosmoxi2d* analysis. Experimenting with a few other cases, we find the mapping $\sigma^2_{FOG} = 1.5\sigma^2_{v_{g-h}}$ to be a good predictor for the best fit *cosmoxi2d* nuisance parameter. Thus we adopt a Gaussian prior on $\sigma^2_{FOG} = 29 \pm 10$ Mpc^2 and recompute DR11 large scale constraints in the case assuming a ΛCDM expansion history, where Samushia et al. (2013) originally found $f\sigma_8 = 0.447 \pm 0.028$. With the new σ^2_{FOG} prior, the constraint shifts to $f\sigma_8 = 0.457 \pm 0.025$. The modest reduction in the uncertainty

is not surprising, since the original hard prior on σ^2_{FOG} (0-50 Mpc^2) was only slightly broader than the new prior. The small shift in the central value comes from the new prior eliminating the lowest end of the originally allowed range of $f\sigma_8$; the small-scale clustering requires satellite galaxies, and thus non-zero σ^2_{FOG}. One important difference between the small-scale and large scale analyses is the use of FKP weights in the latter; we therefore verified that we recover very similar small-scale clustering when applying the FKP weights, so that our derived prior on σ^2_{FOG} remains valid for an FKP weighted correlation function used to analyse large scales.

8   IMPLICATIONS FOR MODIFIED GRAVITY MODELS

Substantial research efforts have recently been devoted to exploring modifications of gravity as a means to explain the apparent cosmic acceleration (Clifton et al. 2012). Schmidt, Vikhlinin, & Hu (2009) showed that for the $f(R)$ model, constraints on non-linear scales, in this case from clusters, are 10^4 times stronger than those obtained on quasi-linear scales. Recently, the velocity structure around massive halos on 1-30 Mpc scales has been identified as a promising observational probe of modified gravity models, both for $f(R)$ models with the chameleon screening mechanism (Lam et al. 2012, 2013; Zu et al. 2013) and a galileon model with the Vainshtein screening mechanism (Zu et al. 2013). In both the $f(R)$ and galileon models studied by Zu et al. (2013), the infall velocity around 10^{14} h^{-1} $M_\odot$ halos at $z = 0.25$ was enhanced by $\sim 20 - 40\%$ on scales of 5 h^{-1} Mpc, the real space halo-matter cross-correlation function showed a scale-dependent enhancement, peaking at $\sim 40\%$ at 2 h^{-1} Mpc, and velocity dispersions increased as well. All three effects would propagate to our $\hat{\xi}_{0,2}$ observable, and we would expect modifications of the same order. Lam et al. (2012, 2013) frame this gravity test in combination with weak lensing, used to measure the mass of the central halos; Zu et al. (2013) showed that similar deviations persist in abundance matched samples of halos. While we plan to incorporate galaxy-galaxy lensing constraints on halo masses in future work (Leauthaud et al. prep), one can still search for the signatures of modified gravity using our measurements, but comparing to clustering-amplitude matched halo samples. The overall amplitude of galaxy clustering observed in our sample constrains the product of the mean halo bias (determined by the galaxy HOD) and the amplitude of matter fluctuations at the effective redshift of the galaxy sample, $b(M, z_{eff})\sigma_8(z_{eff})$. Thus, for a given modified gravity model (realized with an N-body simulation), the HOD would be constrained by the same procedure as we have implemented here for the case of general relativity. With the overall amplitude of clustering matched on $\sim$ 30 Mpc scales, the modifications to the pairwise infall velocities and dispersions will propagate to scale-dependent changes in our $\hat{\xi}_{0,2}$ observables. While we are unable to provide any quantitative constraints without halo catalogs derived from modified gravity simulations, the $\sim 2.5\%$ precision of our GR-based $f\sigma_8$ constraint should severely limit the types of modifications described above.

9   CONCLUSIONS AND FUTURE PROSPECTS

We have made the most precise comparison to date between the observed anisotropic clustering of galaxies at relatively small separations ($\sim 0.8 - 32$ h^{-1} Mpc) and the predictions of a standard halo model in the context of ΛCDM. We found good agreement between our simplified, redshift-independent HOD model and our

measurements of both the projected and anistropic clustering on small scales. Our fits constrain the growth rate of cosmic structure at the effective redshift of our galaxy sample: $f\sigma_8(z_{\rm eff} = 0.57) = 0.450 \pm 0.011$. This constraint is consistent with but improves on our DR11 analysis of large scale anistropy (Samushia et al. 2013) by a factor of 2.5. Intriguingly, our result has the same statistical power but is $\sim 1.9\sigma$ low compared with Planck's ΛCDM prediction, $f\sigma_8 = 0.480 \pm 0.010$ (Planck Collaboration 2013).

The competitive statistical precision of our measurement warrants a systematic evaluation of the observational and modeling systematics. For the former, we introduced a new anisotropic clustering statistic $\hat{\xi}_{0,2}$ that does not include information below the fiber collision scale, but approaches the usual multipoles on large scales. We carefully assessed the systematic and observational uncertainties from the angular upweighting method to correct fiber collisions to order to estimate the projected correlation function $w_p(r_\sigma)$. We combined these measurements to obtain robust joint constraints on the halo occupation distribution and growth rate of cosmic structure probed by CMASS galaxies.

To assess the robustness of our modeling assumptions, we investigated several generalizations to our HOD assumptions and particularly how we assign velocities to the mock galaxies from which we draw our theoretical predictions; the results are summarized in Table 4. The variations we examined caused at most $\sim 0.5\sigma$ shifts in the $f\sigma_8$ constraints. However, given the statistical precison of our reported constraint, further investigation with more sophisicated modeling of the galaxy-halo connection is warranted. Of the possibilities we explored, a model that relaxes the assumption that halos hosting satellite galaxies also host centrals (labelled "cen/sat test") improved the fit to our measurements by $\Delta\chi^2 = 10$ but did not shift $f\sigma_8$ constraints appreciably. Such a model is well-motivated by our target selection process – both color cuts and photometric errors cause massive galaxies to scatter in and out of the sample. Alternatively, we can also improve the model fit by increasing the satellite galaxy velocity dispersion at fixed halo mass.

At least within the cosmological parameter space we explored, we found that for two different definitions of the central galaxy velocity, the data prefer $\mathbf{v}_{\rm DENS}$, the motion of the densest $\sim 0.2r_{\rm vir}$ clump, over $\mathbf{v}_{\rm COMV}$, the halo center-of-mass velocity averaged over all particles within $\Delta_m = 200$. A comparison of these two velocity fields also indicates a possible shift of $\sim 1.5\%$ in the effective large scale $f\sigma_8$, and should therefore be considered when this level of precision is reached.

While we have not tested any explicit modified gravity models, we have shown that the clustering of few $\times 10^{13}$ h^{-1} Mpc halos are consistent with the expectations of ΛCDM and a simple picture of galaxy formation in which halo mass is the only relevant variable determining the probability of hosting a CMASS galaxy. To quantify the precision of this test, our best fit model matches the observed $\hat{\xi}_0$ at the 3 per-cent level from 0.8 - 32 h^{-1} Mpc, and 15 to 5 per-cent level from 5 to 32 h^{-1} Mpc for $\hat{\xi}_2$, with reasonable agreement compared to our uncertainties on smaller scales as well.

As the example of $f(R)$ shows, modified gravity could potentially dramatically alter structure growth on these scales, and our analysis should be used to constrain such models. In addition to the $f\sigma_8$ constraint afforded by our measurements, more precise galaxy velocity bias predictions in ΛCDM would allow our joint constraints on $\gamma_{\rm IHV}$ and $b\sigma_8$ to be interpreted as an additional consistency test between the halo mass inferred from clustering amplitude $b\sigma_8$, and from the halo virial velocities probed by $\gamma_{\rm IHV}$.

Finally, even ignoring the information of the small-scale clustering on $f\sigma_8$, our data tightly constrain the impact of the intra-

halo motions of galaxies on clustering at relatively large scales. We derive a prior on the "finger-of-god" nuisance parameter that is tighter but consistent with the prior adopted in Reid et al. (2012) and Samushia et al. (2013). Moreover, our detailed study of the clustering on small scales also allowed us to validate that $\sigma_{\rm FOG}^2$ as defined in those works can precisely describe the impact of intra-halo velocities of CMASS galaxies on quasi-linear scales.

APPENDIX A: REDSHIFT EVOLUTION OF $\hat{\xi}_{0,2}$

Throughout this analysis we have treated the CMASS sample within $0.43 < z < 0.7$ as a single population. One reason for this is that fiber collision corrections using the angular upweighting become substantially more uncertain as the spectrosopic sample becomes a smaller subset of the target sample. However, the nearest neighbor correction method should be valid in arbitrary redshift bins. Fig. A1 shows our measurement of $\hat{\xi}_{0,2}$ using the nearest neighbor redshift correction for redshift cuts that split the sample equally into three bins in both the north and south. These bins
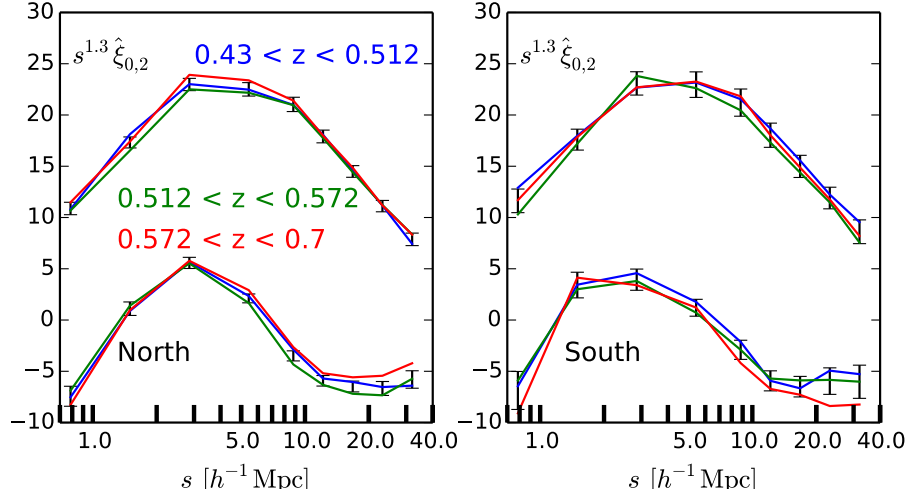
Figure A1. $\hat{\xi}_{0,2}$ measured using the nearest neighbor fiber collision correction method for three redshift subsamples with equal numbers of galaxies, computed separately in the north and the south. Remarkably, our target selection algorithm selects galaxies with very similar clustering across the redshift range of our sample, even though the linear growth factor increases by 14% in our fiducial cosmology between $z = 0.7$ and $z = 0.43$. The black error bars indicate our measurement of $\hat{\xi}_{0,2}$ for the full sample; the error bars shown are the square root of the diagonal elements of the measurement covariance matrix for the full sample, after rescaling it by the fraction of galaxies in the north or south and multiplying by a factor of 3 to approximately indicate the level of scatter expected between the redshift slices. Using the same rescaled covariance matrix to assess consistency between the subsamples and full sample, we find $\chi^2 \approx 12 \pm 2$ in each redshift except the high redshift bin in the north ($\chi^2 \approx 33$).

also have different galaxy weighted number densities: $10^4 \bar{n} = 3.4$, 3.4, and 1.5 $(h^{-1}\mathrm{Mpc})^{-3}$. Rescaling the bootstrap covariance matrix derived for the full sample by $N_{\mathrm{tot}}/N_{\mathrm{subsample}}$ to compute an approximate χ^2 difference between the subsamples and the full $0.43 < z < 0.7$ sample, we find these subsample clustering measurements to be consistent with being drawn from the full sample ($\chi^2 \approx 12 \pm 2$), with the exception of the highest redshift bin in the north ($\chi^2 \approx 33$ for 18 bins); comparison with the same bin in the south suggests most of the difference could be cosmic variance rather than a systematic change from the clustering of the full sample. The covariance matrix used for this comparison is approximate and does not include any of our theoretical error budget. Remarkably, our target selection algorithm selects galaxies with very similar clustering across the redshift range of our sample, even though the linear growth factor increases by 14% in our fiducial cosmology between $z = 0.7$ and $z = 0.43$.

APPENDIX B: SENSITIVITY TO THE HALO CENTRAL VELOCITY DEFINITION

Using the MedRes simulation box, we explore in the left panel of Fig. B1 the mean square velocity difference between the halo center of mass velocity and various central velocity definitions, in units of the halo velocity dispersion: the velocity of the particle at the potential minimum (red), the velocity averaged over the innermost 10 and 20 particles (green), the velocity averaged over a fixed fraction of the innermost halo members, ranging from 3.75% to 40% (blue), and the fiducial choice adopted in this work (thick black dashed line) and detailed in Sec. 2.4. The right panel demonstrates that the mean square dispersion of the central velocity depends on the fraction of innermost halo particles used to determine the central velocity (blue curve). For uncorrelated intrahalo motions, we would expect the green curve; we interpret the difference (red curve) as evidence for bulk motion of the central galaxy. This naive noise

estimate suggests that our fiducial central velocity definition has a sizeable contribution from particle noise. We integrate the square velocity difference in the central velocity dispersion between our MedRes and HiRes simulations (lower dashed and solid curves in Fig. 10) over the best fit HOD, and find only a 13% excess in the MedRes simulation. Since the HiRes mass resolution is eight times larger, we are therefore confident that our central galaxy velocities are negligibly affected by resolution in the mass range of interest for this analysis.

However, since their is no apparent convergence of the central velocity dispersion at small smoothing scales, we expect our predictions for galaxy clustering to be sensitive to this choice. In Sec. 2.4 we argued that our fiducial choice corresponds to the typical galaxy size for the population we are modeling, at least over the halo mass range that dominates the clustering signal. Moreover, our fiducial choice provides approximately the correct amount of central velocity dispersion to match the observed $\hat{\xi}_{0,2}$; slight modifications to the central velocity definition may improve the fit on small scales. We have not explored this possibility further here, but hope to in future work. We note that the final test in Sec. 7.6 showed that our measurements do not favor additional random central velocity dispersion. Examination of hydrodynamic galaxy formation simulations would shed light on both the impact of baryonic effects and could determine the best algorithm to estimate the central galaxy velocity from dark matter-only simulations.

Finally, we note that a similar effect was discussed in Behroozi, Wechsler, & Wu (2013); their Figure 11 includes the *median* three-dimensional velocity offset at $z = 0.53$ in halo mass bins, but averaged in spherical shells rather than including all particles within a given radius. Nonetheless, from their plots we would expect $\sim 55(125)$ km s^{-1} for 10^{13} and 10^{14} $M_\odot$ halos, averaged over 0.06 (0.12) Mpc, while our measurements shown in Fig. 10 predicts ~ 110 (237) km s^{-1} for the rms three-dimensional rms velocity at this redshift. In addition, we find the one-dimensional velocity distribution of $v_{x,\mathrm{DENS}} - v_{x,\mathrm{COMV}}$ to be approximately exponential, for
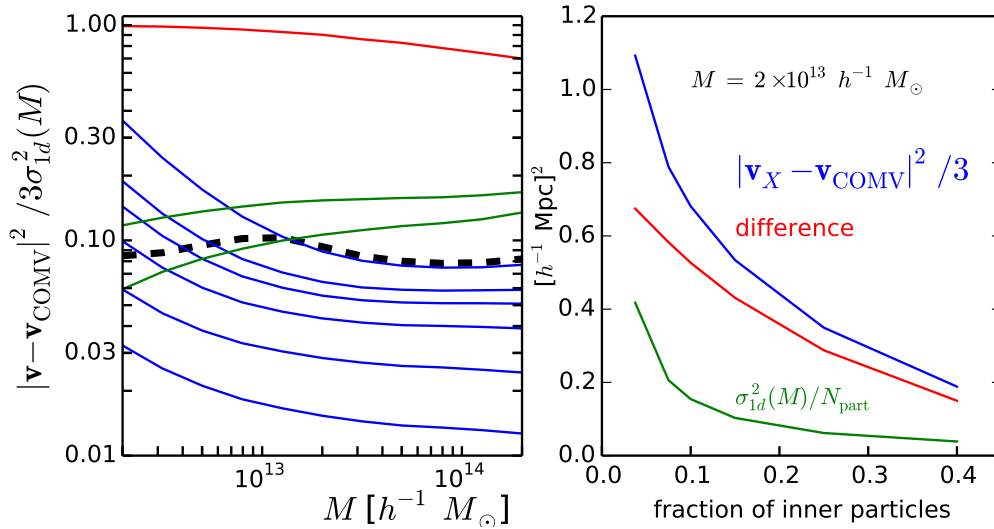
Figure B1. Square differences between $\mathbf{v}_{\mathrm{COMV}}$, the halo center of mass velocity, and various other definitions of the "central" velocity measured from our MedRes simulation. In the left panel we normalize by $3\sigma_{1d}^2(M)$, the three-dimensional halo velocity dispersion averaged over all halo members. The thick dashed black curve shows the fiducial "central" definition detailed in Sec. 2.4 and adopted throughout for our analysis. For ease of comparison with other work, for all other curves we define the center by the minimum of the potential; we verified that the two centers have negligible offsets (0.01-0.02 h^{-1} Mpc). To compute the red curve we simply take the velocity of the particle at the potential minimum; the dispersion of this particle is the same as the average halo particle at low masses and slightly lower in high mass halos. The green curves are computed by averaging over the nearest 10 and 20 particles. The blue curves average over a fixed fraction of the innermost halo members: 0.0375, 0.075, 0.1, 0.15, 0.25, and 0.4 from top to bottom. The right panel shows how the one-dimensional square difference depends on that fraction (blue curve) for the halo mass bin $M = 2 \times 10^{13}\ h^{-1}\ M_{\odot}$. If velocities of the innermost particles were uncorrelated (i.e., there were no bulk motion) and they had the same dispersion as the full halo member population ($\sigma^2(M)_{1d}$), then we would expect a much smaller value for this measurement (green line). The red curve is the difference of the two, indicating a significant bulk velocity relative to the center-of-mass. The amplitude of the central bulk velocity depends on the averaging scale, with no apparent convergence on small scales. Results are similar for other mass bins, with the noise contribution getting smaller at larger halo masses.

which we expect the rms to be larger than the median by a factor of $\sqrt{2}/\ln 2 \approx 2.04$. Therefore the amplitude of the bulk velocities in this work seems consistent with that found in Behroozi, Wechsler, & Wu (2013) using the ROCKSTAR halo finder with slightly higher mass resolution.

REFERENCES

Ade P. et al., 2013, arXiv:1303.5076
Ahn C., et al., 2014, ApJS, 211, 17
Aihara H., et al., 2011, ApJS, 193, 29
Alcock C., Paczynski B., 1979, Nature, 281, 358
Anderson L., et al., 2013, arXiv:1312.4877
Behroozi P., Wechsler R., Wu H., 2013, ApJ, 762, 109
Benson A., Cole S., Frenk C., Baugh C., Lacey C., 2000, MN-RAS, 311, 793
Berlind A., Weinberg D., 2002, ApJ, 575, 587
Beutler F., et al., 2013, arXiv:1312.4611
Blanton M., et al., 2003, AJ, 125, 2276
Bolton A., et al., 2012, AJ, 144, 144
Cacciato M., van den Bosch F., More S., Mo H., Yang X., 2013, MNRAS, 340, 767
Chuang et al., 2013, arXiv:1312.4889
Clifton T., Ferreira P., Padilla A., Skordis C., 2012, Physics Reports, 513, 1
Cohn J., White M., 2013, arXiv:1311.0850
Conroy C., Wechsler R., Kravtsov A., 2006, ApJ, 647, 201
Cooray A., Sheth R., 2002 Physics Reports, 372, 1

Davis M., Efstathiou G., Frenk C., White S., 1985, ApJ, 292, 371
Dawson K., et al., 2013, AJ, 145, 10
de al Torre S., 2013, A&A, 557, 54
Eifler T., Kilbinger M., Schneider P., 2008, A&A, 482, 9
Eisenstein D.J., et al., 2011, AJ, 142, 72
Fisher K.B., 1995, ApJ, 448, 494
Gao L., Springel V., White S., 2005, MNRAS, 363, 66
Gunn J.E., et al., 1998, AJ, 116, 3040
Gunn J.E., et al., 2006, AJ, 131, 2332
Guo H., et al., 2014, arXiv:1401.3009
Guo H., Zehavi I., Zheng Z., 2012, ApJ, 756, 127
Hartlap J., Simon P., Schneider P., 2007, A&A,464,399
Hawkins E., et al., 2003, MNRAS, 346, 78
Hikage C., 2014, arXiv:1401.1246
Kaiser N., 1987, MNRAS, 227, 1
Keisler R., Schmidt F., 2013, ApJ, 765, 32
Komatsu E., et al., 2011, ApJS, 192, 18
Jackson J., 1972, MNRAS, 156, 1P
Krause E., 2013, MNRAS, 428, 2548
Lam T., Nishimichi T., Schmidt F., Takada M., 2012, PhRvL, 109, 1301
Lam T., Schmidt F., Nishimichi T., Takada M., 2013, PhRvD, 88, 023012
Landy S.D., Szalay A.S., 1993, ApJ 412, 64
Leauthaud A., et al., in prep.
Limber D., 1954, ApJ, 119, 655
Li C., Kauffmann G., Jing Y., White S., Börner G., Cheng F., 2006, MNRAS, 368, 21
Mandelbaum R., Slosar A., Baldauf T., Seljak U., Hirata C., Naka-

jima R., Reyes R., Smith R., 2013, MNRAS, 432, 1544

Marin F., et al., 2011, ApJ, 737, 97

Marinoni C., Hudson M., 2002, ApJ, 569, 101

Masters K. et al., 2011, MNRAS, 418, 1055

Neistein E., Khochfar S., 2012, arXiv:1209.0463

Norberg P., Baugh C., Gaztañaga E., Croton D., 2009, MNRAS, 396, 19

Nuza et al., 2013, MNRAS, 432, 743

Parejko J., et al., 2013, MNRAS, 429, 98

Peacock J., Smith R., 2000, MNRAS, 318, 1144

Piloyan A., Marra V., Baldi M., Amendola L., arXiv:1401.2656

Reid B., et al., 2012, MNRAS, 426, 2719

Reid B., Spergel D., 2009, ApJ, 702, 249

Reid B., White M., 2011, MNRAS, 417, 1913

Reyes R., 2010, Nature, 464, 256

Ross A. et al., 2012, MNRAS, 424, 564

Ross A. et al., 2014, MNRAS, 437, 1109

Ross N., et al., 2007, MNRAS, 381, 573

Samushia L., et al., 2013, arXiv:1312.4899

Sanchez A., et al., 2013, arXiv:1312.4854

Schmidt F., Vikhlinin A., Hu W., 2009, PhRvD, 80, 083505

Sheth R., 2005, MNRAS, 364, 796

Seljak U., 2000 MNRAS, 318, 203

Seo H. J., Eisenstein D., Zehavi I., 2008, ApJ, 681, 998

Tinker J., 2007, MNRAS 374, 477

Tinker J. et al., 2012, ApJ, 745, 16

Tinker J., Kravtsov A., Klypin A., Abazajian K., Warren M., Yepes G., Gottlʹober S., Holz D., 2008, ApJ, 688, 709

Tinker J., Robertson B., Kravtsov A., Klypin A., Warren M., Yepes G., Gottlʹober S., 2010, ApJ, 724, 878

White M., et al., 2011, ApJ, 728, 126

White M., Cohn J., Smit R., 2010, MNRAS, 408, 1818

White M., Hernquist L., Springel V., 2001, ApJ, 550, 129

White M., Padmanabhan N., 2009, MNRAS, 395, 2381

Vale A., Ostriker J., 2006, MNRAS, 371, 1173

van den Bosch F., More S., Cacciato M., Mo H., Yang X., 2013, MNRAS, 430, 725

van den Bosch F., Weinmann S., Yang X., Mo H., Li C., Jing Y., 2005, MNRAS, 361, 1203

Wang L., Weinmann S., De Lucia G., Yang X., 2013, MNRAS, 433, 515

Wu H., Hahn O., Evrard A., Wechsler R., Dolag K., 2013, MNRAS, 436, 460

Yang X., Mo H., Jing Y., van den Bosch F., 2004, MNRAS, 350, 1153

Yang X., Mo H., van den Bosch F., MNRAS, 339, 1057

Yang X., Mo H., van den Bosch F., 2009, ApJ, 695, 900

York D.G., et al., 2000, AJ, 120, 1579

Zehavi I. et al., 2011, ApJ, 736, 59

Zentner A., Hearin A., van den Bosch F., 2013, arXiv:1311.1818

Zheng Z., et al., 2005, ApJ, 633, 791

Zu Y., Weinberg D., Jennings E., Baojiu L., Wyman M., 2013, arXiv:1310.6768

Zu Y., Weinberg D., 2013, MNRAS, 431, 3319